2010

Neural Network Based Torque Control of Switched Reluctance Motor for Hybrid Vehicle Propulsion

Dongyun Lu
University of Windsor

NEURAL NETWORK BASED TORQUE CONTROL OF SWITCHED RELUCTANCE MOTOR FOR HYBRID ELECTRIC VEHICLE PROPULSION

By

Dongyun Lu

A Thesis

Submitted to the Faculty of Graduate Studies

through the Department of Electrical and Computer Engineering

in Partial Fulfillment of the Requirements for

the Degree of Master of Applied Science at the

University of Windsor

Windsor, Ontario, Canada

2009

DECLARATION OF PREVIOUS PUBLICATION

This thesis includes 2 original papers that have been previously published in peer reviewed proceedings, as follows:

Thesis Chapter	Publication title	Publication status
Chapter 4	Neural network based torque control of switched reluctance motor for hybrid electric vehicle propulsion at low speeds	published
Chapter 5	Neural network based torque control of switched reluctance motor for hybrid electric vehicle propulsion at high speeds	published

I certify that I have obtained a written permission from the copyright owners to include the above published materials in my thesis. I certify that the above material describes work completed during my registration as graduate student at the University of Windsor.

I declare that, to the best of my knowledge, my thesis does not infringe upon anyone's copyright nor violate any proprietary rights and that any ideas, techniques, quotations, or any other material from the work of other people included in my thesis, published or otherwise, are fully acknowledged in accordance with the standard referencing practices. Furthermore, to extent that I have included copyrighted material that surpasses the bounds of fair dealing within the meaning of the Canada Copyright Act, I certify that I have obtained a written permission from the copyright owners to include such materials in my thesis.

I declare that this is a true copy of my thesis, including any final revisions, as approved by my thesis committee and the Graduate Studies office, and that this thesis has not been submitted for a higher degree to any other University or Institution.

ABSTRACT

Considering the extensive non-linearities in the switched reluctance motor (SRM) drive, variation in the DC bus voltage and specific requirements of the hybrid electric vehicles (HEVs) traction application, a feed-forward back propagation neural network (BPNN) based torque controller is proposed. By using proposed controller, the torque ripple has been effectively reduced at low speeds while the power efficiency has been optimized at high speeds range. The problem of multi-valuedness related with the neural network based direct inverse control has been targeted by designing a bank of two-hidden-layer neural network controllers. And the problem of torque oscillation due to the change of control mode and step change of firing angle has been solved by using dead-band filtering and nearly continuous changing of firing angle and phase currents. Computed results are presented to demonstrate the effectiveness of the proposed control scheme.

To My Family

ACKNOWLEDGEMENT

I wish to express my sincere gratitude to my advisor Dr. Narayan Kar for his assistance at every step of the way. His guidance has had an immense influence on my professional growth and without his technical expertise, reviews, and criticism it would not have been possible to shape this thesis. I would also like to thank my committee members Dr. Nie and Dr. Wu for their valuable suggestions and guidance in the completion of this work.

I would like to show my appreciation for my husband, my sons and my dear friends who made strenuous times seem easy and turned stressful days into fun. Their love and support will always be invaluable.

In the end, I want to thank my fellow graduate students in the Electric Machines and Drives Research Lab for their support and encouragement. Working in their friendly company was a memorable experience.

TABLE OF CONTENTS

LIST OF TABLES

LIST OF FIGURES

LIST OF APPENDICES

1   INTRODUCTION

1.1 Background

With constraints on energy resources and concerns over emissions, fuel economy and global warming, hybrid electric vehicles (HEVs) have attracted considerable attention from more and more automakers and customers in which hybrid propulsion helps to improve fuel economy, reduce emissions and enhance the performance of conventional internal combustion engine (ICE). Wells-to-wheels energy analysis shows that the process of delivering 100 units of gasoline energy to the vehicle's fuel tank is 88% efficient for both conventional and hybrid technologies. Conventional gasoline ICEs are approximately 25% efficient with the overall driveline efficiency of 65% which leaves 14 units of energy delivered to the wheels for propulsion. However, [1] states that for a gasoline hybrid drivetrain, 26.4 units of energy are delivered to the wheels, which is 88% more efficient than a conventional vehicle driveline.

Moreover, in the last several decades, the problem of emissions and pollution due to transport is getting worse. With a worldwide trend of increase in population, economic growth, rapid urbanization and industrial development, the demand for transportation is on the rise. Due to the dependency of the transport sector on fossil fuels, the consequent consumption of petroleum is increasing exponentially. Fossil fuel dependency of the rapidly growing transport sector, particularly on-road transportation, and massive increase in petroleum consumption are the main concerns as fuel reserves continue to deplete at an alarming rate. This calls for the research for an alternative fuel vehicle technology to gradually displace gasoline driven vehicles by those powered by more sustainable and environment-friendly fuel options.

A yet more grave consequence of the combustion of petroleum, particularly by on-road transportation is the emission of toxic pollutants including oxides of nitrogen, carbon monoxide, and unburned hydrocarbon particles. These pollutants not only degrade the air quality with a long lasting damaging effect on the environment but also pose risk to public health. Vehicular emissions are also a source of carbon dioxide, the principal

greenhouse gas which is responsible for the global warming that is continuing to cause ecological changes and natural disasters.

Realization of the aforementioned severe effects of extensive fuel combustion has motivated researchers to improve the efficiency of today's on-road transportation. Conventional vehicles powered by ICEs have been used extensively for over 100 years and although efforts continue to improve their fuel efficiency, the long term solution to vehicular emissions and dependence on petroleum products is still relying on the development of renewable energy sources and alternative fuel vehicle technologies. Alternative vehicles refer to the kind of vehicles that are partially or solely powered by sources of energy other than fossil fuels such as bio-fuels, electricity or hydrogen. The target of all such vehicles is to minimize vehicle emission, increase sustainability and reduce strain on the environment.

The way of the electric vehicles to the market is blocked by the development of battery whose limited energy storage capability restricts electric vehicle only to some specific applications such as at airports, railroad stations, on golf courses, etc. In fact, basic study in [2] shows that electric vehicles are hard to challenge the liquid-fueled vehicles even with the optimistic value of battery energy capacity. Thus, in recent years, advanced vehicle technology research has turned to hybrid electric vehicles as well as fuel cell vehicles [3]. As the challenges on the hydrogen production, storage, and distribution are still difficult to overcome, fuel cell-powered vehicles still have long way to go before they can be introduced in the market. Right now, hybrid electric vehicles are the only applicable and affordable solution to the world's demands for lower polluting and more fuel efficient personal transportation.

1.2   Motor Selections for Hybrid Electric Vehicle

1.2.1   Requirements of the HEV Drive Motor

The distinguished difference of operational features between HEVs and conventional automobiles is the electric propulsion system, which consists of an electric motor, power electronic drive for the motor and electronic controllers. With increasing consumer expectation for improved vehicle performance, auto manufacturers are recognizing that design of next generation hybrid propulsion systems will heavily rely on

the development of high performance motors for HEV specific application. This will particularly hold true as motors become the primary traction component to extend the whole electric range of HEV. Although electric motor drive and its control are mature technology, further improvement in efficiency, robustness, weight, cost, noise, vibration and harshness (NVH) of electric motors for HEV traction application can be achieved through modifications in the motor design and control strategies.

Figure 1.1 shows characteristics of electric motors required for the HEV traction application. In the constant torque region, the electric motor delivers constant torque from zero to base speed. Past the base speed, the torque decreases with the speed, maintaining a constant rated power output [4]. Selection of an appropriate traction motor is based on the motor characteristics, such as flexible drive control, high efficiency, power density (power output/volume), reliability, low acoustic, noise and cost, which is a crucial stage in the design of the electric drivetrain that requires special attention. The three main factors that need to be taken into consideration during the selection and design process of motors are a) driver expectation for the driving profile in terms of acceleration demand, climbing and braking performance, maximum speed and range, b) vehicle constraints of weight and volume based on vehicle type and c) the type and specifications of the energy storage unit. An electric motor for hybrid vehicle traction is typically expected to fulfill the following requirements [5]:
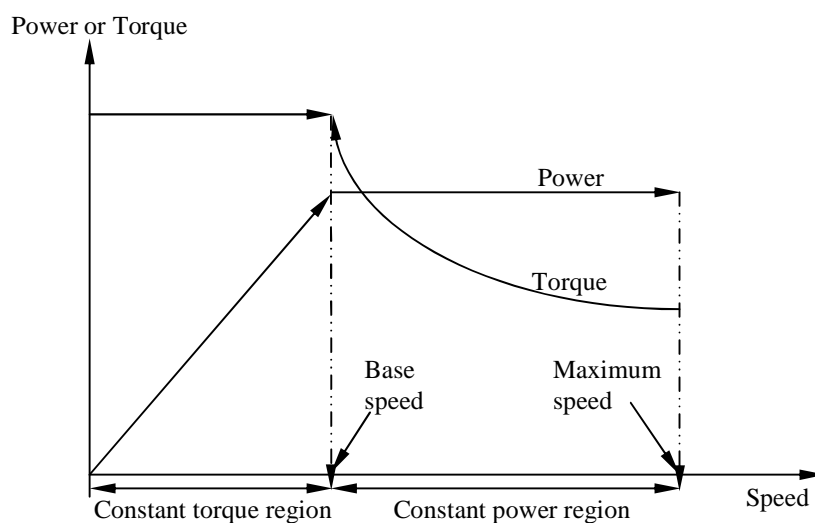
Fig. 1.1 Desired characteristics of electric traction in HEV.

3

- High instant power and high power density

- Fast torque response

- High torque at low speeds for starting and climbing

- High power at high speed for cruising

- Wide speed range in constant-torque and constant-power regions

- High efficiency over the wide speed and torque ranges

- High efficiency for regenerative braking

- High reliability and robustness for various vehicle operation conditions

- Low acoustic noise and electromagnetic interference (EMI)

- Low maintenance and initial cost

Under these criteria, several electric machines are being investigated for HEV traction application. Although DC motors were the initial choice, induction motors (IMs), permanent magnet synchronous motors (PMSMs) and switched reluctance motors (SRMs) have now gained more attention as the favoured candidates for HEV propulsion. Special designed motors for HEV traction application have also emerged. Nowadays, although PMSMs are gaining popularity due to their high power density and packaging flexibility, fail-safe field weakening with a conventional drive has yet to be demonstrated. As each topology has unique integration advantages, due to the requirements of traction motors, which must combine high torque density with high power density, choice of motor type is still not resolved [6].

1.2.2 Motor Characteristics

1.2.2.1 *Permanent Magnet Synchronous Motors*

Permanent magnet synchronous motors (PMSMs) use a rotor made of earth magnetic materials to generate magnetic flux. Depending on the arrangement of the magnet, they can be classified as surface-magnet mounted or buried-magnet mounted. Absence of rotor windings gives PMSMs an edge over induction motors in terms of efficiency [7]. Comparing with IMs and SRMs, they have higher power density, higher efficiency and simpler control method, which make them the primary choice of leading automakers such as Toyota Prius and Honda Insight. Most hybrid cars available commercially today are equipped with PMSMs.

However, the absence of field windings makes the flux weakening capability of PMSMs highly constrained which limit their speed ranges in the constant power region [8] and fail-safe field weakening with a conventional drive has yet to be demonstrated. One method to overcome this limitation is to control the conduction angle of the power converter. An alternative solution is by using PM hybrid configuration where the air-gap magnetic field is obtained through a combination of the magnet and additional field winding. The direction and magnitude of the DC field current can be controlled so as to weaken the flux of the magnet. However, this may result in demagnetization which will decrease the motor efficiency at the very high-speed range.

The negative aspect of using permanent magnet is its sensitivity to temperature. This drawback limits the motor's power/size ratio, requires a complex cooling system and the demagnetization with age can affect long term performance of the machine. Another drawback of PMSM is the high costs and limited resources of permanent magnets. Nevertheless, PMSMs are still a strong contender for HEV and plug-in hybrid electric vehicle (PHEV) drives.

1.2.2.2 Induction Motors

Induction motors, particularly squirrel cage IMs have been widely regarded as one of the most suitable options for HEVs due to their rugged construction, mature control and drive technology, and low cost which make them suitable for operations in the harsh environment of traction drives. Accurate speed control of induction machines is made possible by vector control techniques, and wide speed ranges, generally over two to three time the synchronous speed, can be obtained through flux weakening. Their control and drive technology have well matured and prominent automakers have used IMs in their HEVs and electric vehicles (EVs) including Tesla Roadster, Daimler/Chrysler Durango, Chevrolet Silverado and BMW X5.

However, the IM drives are still facing a number of drawbacks that put them behind the race of HEVs electric propulsion. The breakdown torque creates a limitation on the constant power operation of the motor. If IM runs at speeds higher than the critical value where break down torque is reached, the motor begins to stall [4]. Moreover, the most crucial factor that has diverted auto manufacturers away from IMs is their inherently lower efficiency than PMSMs particularly due to copper losses in the rotor.

Rotor resistance variation due to temperature is also a problem that can detune the field controller during its operation [5].

Research is now focused on addressing these issues through design modification and more effective control methods. A new generation of control strategies are being tested to improve the overall efficiency of induction motors [9] and a multiphase pole-changing IM drive has been developed to extend the constant-power region without over-sizing the motor [10], [11]. By using digital motor controller with a 150 MHz DSP and applying stator flux-oriented vector control, the induction motor in Tesla Roadster is managed to produce a maximum net power of 185 kW at 5,000-8,000 rpm. The maximum speed of this motor is 14,000 rpm and the efficiency can be 92% average with 85% at peak power, and torque output can reach 375 Nm at 0-4,500 rpm [12].

1.2.2.3 Switched Reluctance Motors

SRMs are beginning to gain interest as a potential candidate for HEV propulsion due to their simple and rugged construction, fault tolerant operation, insensitivity to high temperatures, an extremely long constant-power range and high speed operation [13]-[15]. The motor speed-torque characteristics are also excellently matching with the road load characteristics [5], and the performance of SRM for HEVs applications has been found to be excellent.

However, there are several barriers that need to be resolved before they can be applied in mass produced vehicles [16]. Since SRM involves successive excitation of poles to produce continuous motoring or generating torque by aligning the rotor, the motor drive needs a position sensor for high-grade control. Torque ripple, vibration and associated acoustic noise are also the main concerns in SRM operation [17]. These issues are critical in vehicle application and research is targeted towards analysis, design improvement and development of excitation schemes and control strategies to reduce these effects.

Recently, there have been several key technologies that offer solutions for the above issues [13]. One technology is the bipolar excitation which improves efficiency by ensuring short flux path excitation during which the excited phase has a higher inductance as compared with long flux path excitation; the second key technology is the freewheeling control strategy to boost productivity while operating as a generator and the

third one is the four-quadrant sensorless control over entire speed range to eliminate the position sensor.

1.2.2.4 HEV Specific Motor Designs

The auto industry is also looking for more drastic modifications in terms of material selection, innovative component shapes and designs, and control strategies for electric motors to improve efficiency, cost and NVH while maintaining compact size and light weight.

For PMSMs, the major HEV producers such as Honda and Toyota are making progress in the design of motor and drive. Honda, for example, has developed an exceptionally thin (70 mm) PMSM for their Civic Hybrid, shown in Fig. 1.2(a), which claims to have achieved a peak efficiency of 97%. Figure 1.2(b) shows a 3D motor developed by Nissan for HEVs with a modified deign for maximum utilization of magnetic flux [18].

Toyota has made historical progress in the power density of the PMSM for Toyota Hybrid System (THS) II as shown in Fig. 1.3(a) without increasing the motor size by (1) increasing the motor maximum speed by using DC-DC boost-up converter to increase DC-link voltage, (2) installing the superior cooling system using Automatic Transmission Fluid (ATF), and (3) applying series winding in stators [19]. Another hybrid excitation motor using less rare-earth magnet to obtain high power density, as shown in Fig. 1.3(b), has been presented in [20] which reduces the volume of permanent magnet by approximately half of that used in an existing IPMSM for LEXUS RX400h

(a)   (b)
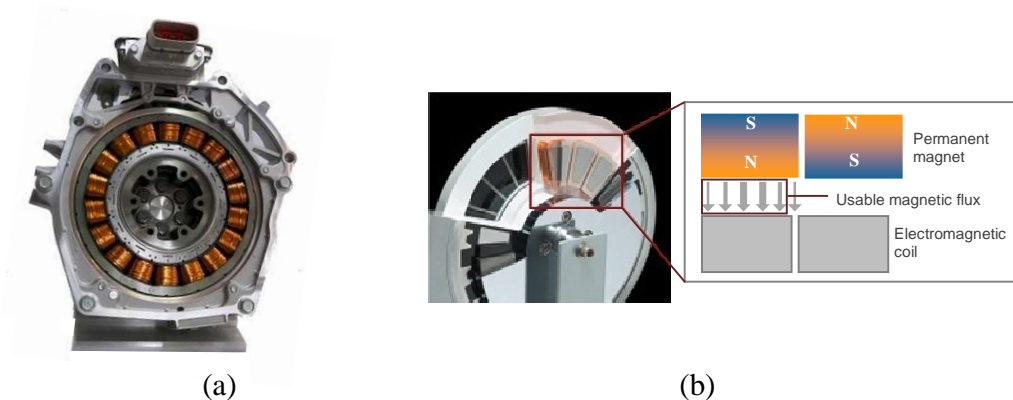
Fig. 1.2 Special motor designs for HEVs.
(a) PMSM in Honda Civic Hybrid. (b) Nissan's 3D PM motor.

7
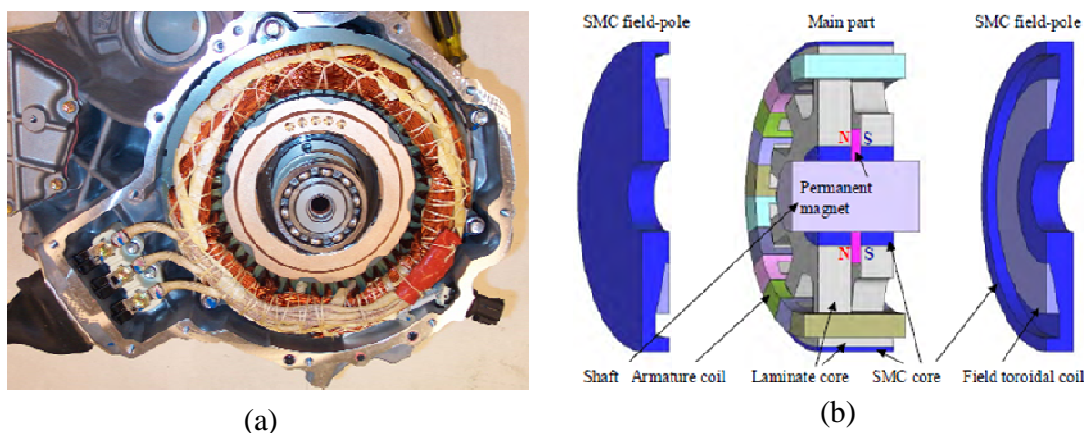
Fig. 1.3 Special motor designs for HEVs. (a) Traction motor for THS II. (b) New motor design with half of permanent magnet.

while keeping the power density intact. Major Differences between the conventional PM machines and the proposed machine are (1) the rotor with the permanent magnet is sandwiched by N- and S-pole rotor core and is magnetized in the axial direction similar to the conventional hybrid stepper machine (2) the field pole core, made of Soft Magnetic Composites (SMC) with toroidal field coil, is jointed at each end of the machine in the axial direction.

Researchers are also developing "hub" style induction motors of much smaller dimensions for the same power output as shown in Fig. 1.4(a). New designs of SRM have also been proposed in [21] for HEV applications. By applying five-phase 15/12 and pancake shape shown in Fig. 1.4(b), the motor exhibits lower torque ripple and higher power density comparing with the conventional rotary SRMs. All these efforts are directed towards improving the power efficiency, power density and torque outputs of motors while maintaining smooth operation, light weight and compact structure, and within a reasonable cost.

(a)   (b)
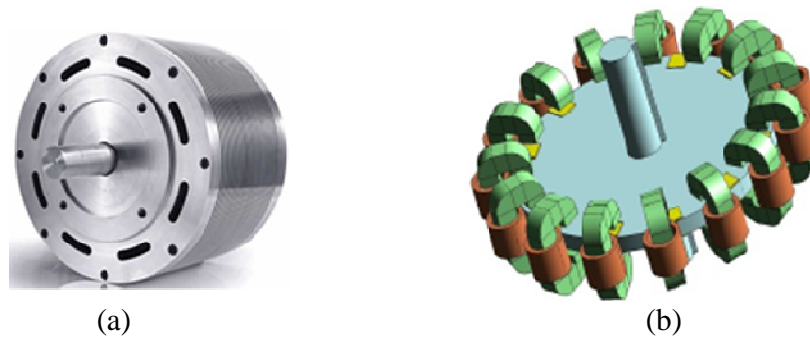
Fig. 1.4 Special motor designs for HEVs.
(a)Hub Hub style induction motor, (b) New SRM design

1.3   Literature Review

Currently, HEVs typically employ PMSMs due to their high power density and packaging flexibility; however, due to the unique requirements of traction motors, which must combine high torque density with high power density, choice of motor type is still not resolved. Recently, switched reluctance motors (SRMs) have attracted interest for HEV propulsion for their robust construction, fault tolerant operation, high starting torque without the problem of excessive inrush current, and ability to extremely high-speed operation. However, SRM suffers from some drawbacks such as high torque ripple and acoustic noise which are quite critical for HEV applications. The development of an optimal control scheme is difficult for SRM to reduce torque ripple and optimize the power efficiency in the whole speed range due to the high non-linearity existed in the torque-current-position characteristics for its saturation region of operation.

1.3.1   Torque Control with Torque Ripple Reduction

Extensive work has been done to minimize torque ripple in SRM for general applications [22]-[28]. In [24], a Cerebellar Model Articulation Controller (CMAC) based torque control was presented. A close-loop torque controller based on B-spline neural network (BSNN) with online training was presented in [25]. But both CMAC and BSNN suffer from higher memory demand [29].

Back-propagation (BP) based neural network controllers have been proposed in [26]-[28], but both [26] and [27] used one-hidden-layer neural network which is not

sufficient for stabilization and [28] did not consider the effect of multi-valuedness on the neural network mapping which could not produce high accuracy mapping [30].

Due to considerable non-linearity in the torque characteristics of SRM, the extensive requirement for lower torque ripple, good dynamic performance and cost sensitivity of the HEV traction application, most of the techniques discussed in the literature for this specific application are based on look-up table [31], [32]. In [31], look-up tables were generated off-line by building an SRM model to profile the current for the flat torque waveform and stored in the controller. During on-line running, the controller searched the look-up tables for the current command. Another comprehensive controller to maximize efficiency and peak overload capability of SRM by using look-up tables for electric vehicle drives has been designed in [32]. This controller has several look-up tables for different voltages. To calculate the control parameters for a certain torque-command/rotor-speed (operating point) and bus voltage, three interpolations have to be performed. As these interpolations are linear, they are subject to errors depending on the resolution of each table and the number of tables stored for different voltages. To overcome the above problem and also to reduce the table access time for interpolation, square tables are generated for each bus voltage. But still, there is a trade-off between the memory needed, execution time and the error rate. If the discretion steps of the rotor position and torque output are very small, the ideal current for minimizing the torque ripple will be found, but the amount of data will be enormous which needs a large memory and very long search time. On the other hand, if the discretion steps are big, the ideal current needed for reducing torque ripple may not be found. Unfortunately, at low speed, the torque ripple is sensitive to the current profile, and a slight deviation from the required profile may produce high torque ripple.

1.3.2   Torque Control with Efficiency Optimization

The electric motor drivetrain includes battery, motor, converter and control algorithm. Due to the variable DC bus voltage caused by the variation in the state-of-charge (SOC) of the battery and the nonlinearities found both in the motor and the switching converter [33], the torque control for switched reluctance motor while optimizing the motor efficiency for traction application becomes very complex.

As the motor losses are proportional to the motor speed, they have to be reduced at the high speed range to improve the motor efficiency. Extensive works have been done to optimize the efficiency of SRM at high speeds [32]-[36]. In [34], a general theory to find the optimal turn-off and turn-on angles in order to maximize efficiency is developed based on the energy conversion loops for both voltage control and current control without considering the variation in the battery voltage. A general method to find the optimal turn-off angle is also defined in [35] based on the critical rotor position that the flux linkages of two neighboring phases (outgoing and incoming phases) are equal to half of the flux linkage peak value. But both [34] and [35] did not take the nonlinearity of the switching loss in the converter into consideration.

Look-up tables have also been studied to maximize efficiency in [36]. In [36], turn-on angles searching strategy for optimizing the drive efficiency of SRM is proposed based on the mathematical model of the motor drive including the power losses from the SRM and converter. After the searching ended, a synthesized look-up table to map the torque, speed, and DC-bus voltage with a set of duty ratio, turn-on and turn-off angles is obtained and used in real time controlling. However, there is a trade-off between the memory needed, execution time and the error. Significant errors may be introduced due to the linear nature of these interpolations, especially if inadequate data are stored due to the lack of available memory.

Contributing to the ability to learn, recall and generalize from training patterns or data, neural network has become an effective control method. A Cerebellar Model Articulation Controller (CMAC) based torque control was presented in [24]. The approach allows the generation of optimal current profiles in terms of minimizing torque ripple, copper loss and rate of change of current as the motor runs at high speeds that ensures the minimization of torque ripple while having high power efficiency. But CMAC suffers from higher memory demand as demonstrated in [29].

1.4   Research Objectives

The ultimate goal for this research is to design a neural network strategy based torque controller of the SRM drive for HEV traction application over the whole speed range, simulate the proposed torque control system by using MATLAB/SIMULINK,

investigate the performance and analyze the results. In this research, a novel SRM torque control method based on a bank of feed-forward back propagation neural networks (BPNNs) is developed to track the torque command from the energy management system of HEV. Direct inverse control is applied for its simple, easy to implement and fast dynamics. Special data pre-processing technique has also been used to handle the problem of multi-valuedness.

As there are two different objectives for the whole speed range: to reduce the torque ripple at low speeds and to optimize the energy efficiency at high speeds, two controllers have been designed to deal with the situation. At low speeds, two-phase excitation and torque sharing function have been used to reduce the torque ripple. After torque sharing function has been used to distribute the torque command into two phases, a set of BPNNs are then trained to learn the current profiles based on the static torque characteristics. During real-time operation, the phase currents will be calculated through the BPNNs and applied to the hysteresis current controller. Gate signals generated from the current controller will be applied to the asymmetric bridge converter to excite the SRM.

At high speeds, considering the extensive non-linearities in the converter and torque characteristics of SRM, variation in the DC bus voltage, the extensive requirement for high efficiency, good dynamic performance and cost sensitivity of the HEVs traction application, a BPNN based direct inverse control is proposed to track the torque command while optimizing the motor efficiency. A set of switching angles corresponding to the specified operating points with maximum efficiency have been used to train the neural networks. After training, the NN controller occupies the ability to calculate the switching angles in real-time operation. Based on the switching angles calculated, the commutation logic decides the phases to be excited to track the torque and speed command from the energy management system of the HEV.

Due to the two different control methods used at low speeds and high speeds, specific considerations will be taken to ensure smooth torque output when the demanded motor speed is jumped from lower speeds (< base speed) to higher speeds (>base speed).

1.5 Thesis Outline

This thesis is organized as follows:

Chapter 2: Switched reluctance motors are discussed in detail as a highly suitable candidate for HEV propulsion. This chapter discusses their construction, statistic characteristics and torque production mechanism in detail. Analysis of the power losses is also presented in this chapter. The control principles of torque control such as voltage control and current control are also presented.

Chapter 3: This chapter describes the history of the neural network. The knowledge about the back propagation neural network such as architecture, algorithm, training method, types of activation function, problems related with the decision of number of hidden layers and application procedure are going to be presented in detail.

Chapter 4: A neural network based torque controller to minimize the torque ripple at low speeds will be described in this chapter. Simulation results are presented to demonstrate that the proposed controller provides good dynamic performance with respect to changes in torque commands. The controller also satisfies the HEV propulsion requirements during starting.

Chapter 5: In this chapter, a neural network based torque controller to optimize the power efficiency at high speeds will be described. Simulation results are presented to demonstrate that the proposed controller provides good dynamic performance with respect to changes in operation points while optimizing the motor efficiency.

Chapter 6: A neural network based torque controller for the whole speed range will be described in this chapter. Special considerations on the torque/speed oscillation related with the change of the control mode are discussed. Simulation results are presented to demonstrate that the proposed controller provides good dynamic performance.

Chapter 7: This chapter summarizes the work done and future research in this area.

2 MODELLING AND ANALYSING OF SRM

2.1 Introduction

The switched reluctance motor (SRM) is a doubly salient machine where both stator and rotor have salient poles. It is a singly exited reluctance machine with independent phase windings on the stator and no windings on the rotor, and it is also a type of synchronous machine which has wound field coils of a DC motor for its stator windings and has no coils or magnets on its rotor. Its torque is produced by the tendency of the moveable part to move to a position where the inductance of the excited winding is maximized. A cross-sectional diagram of a four-phase 8/6 SRM is shown in Fig. 2.1. The performance index can be cost, efficiency, weight, volume, torque, output, or a combination of these for the switched reluctance motor and converter combination.

2.2 Physical Construction of SRM

The rotor has no permanent magnet on it. Stator windings on diametrically opposite poles are connected in series or parallel to form one phase of the motor. Several combinations of stator and rotor poles are possible, such as 6/4 (6 stator poles and 4 rotor poles), 8/4, 10/6 and 12/6. The configurations with higher number of stator/rotor pole combinations have less torque ripple.

By the nature of the motion, the SRM can be rotary or linear as shown in Fig. 2.2. If the motor is running in rotating mode, it is called a rotary SRM, or else called linear SRM. The rotary machine-based SRM is further differentiated to radial field SRM and axial field SRM by the direction of the magnetic field path with respect to the axial length
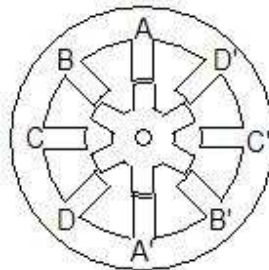
Fig. 2.1 Four-phase 8/6 SRM configuration.

of the machine, when the magnetic field path is perpendicular to the shaft, it is classified as a radial field SRM, otherwise, it is an axial field SRM [37].

Radial field SRMs can be classified as short and long flux path SRMs. When the coils are placed in the diametrically opposite slots, it is called a long flux path SRM. The other kind of radial field SRMs is called a short flux path SRM whose phase coils are placed in the slots adjacent to each other to obtain a pair of poles. The comparison of characteristics of these two kinds of SRMs is presented in Table 2-1.

Axial field SRM can be further differentiated into single-stack and multi-stack SRMs. A pair of one rotor and one stator stacks or one rotor and two stator stacks or two rotor and one stator stacks constitutes a single-stack axial field SRM. Multiples of such single stacks can be arranged on the same shaft to augment the power rating, which is called a multiple-stack axial field SRM, invented in the early 1970s for electric vehicle propulsion [38]. The axial field SRMs are ideal for applications where the total length maybe limited such as the vehicle propulsion application. The disadvantage of this configuration is that the stator laminations have to be folded one on top of the other unlike the simple stacking of laminations in the radial field configuration.
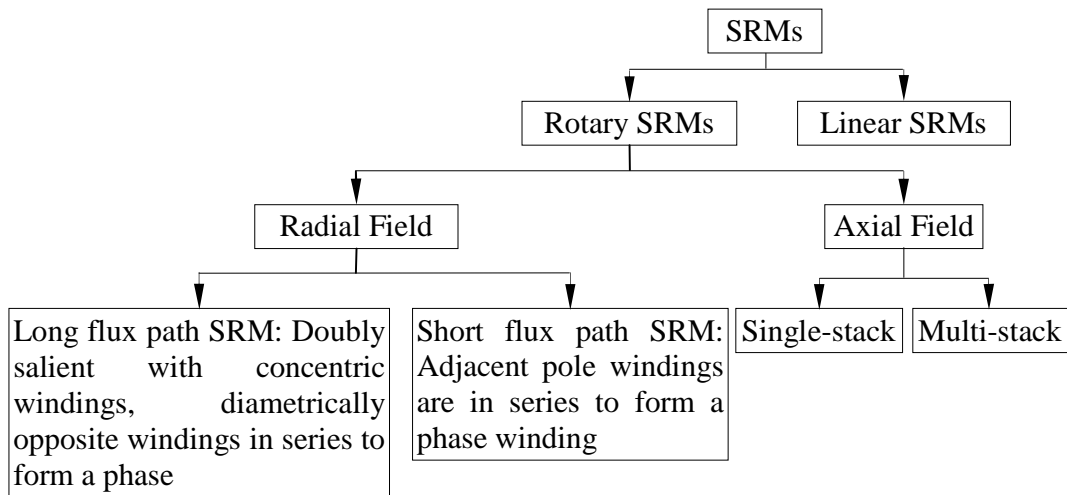
Fig. 2.2 Classification of SRMs.

Table 2-1 Comparison of characteristics of short and long flux path SRMs

	Core losses	Mutual inductance	Radial force
Short flux path SRM	lower	higher	higher
Long flux path SRM	higher	lower	lower

2.3 Equivalent Circuit

An elementary equivalent circuit of an SRM can be derived neglecting the mutual inductance between the phases as following [37]:

$$V = R_s i + \frac{d\{L(\theta,i)i\}}{dt}$$
$$= R_s i + L(\theta,i)\frac{di}{dt} + i\omega_m \frac{dL(\theta,i)}{d\theta}$$

(2.1)

where R_s is the phase resistance,

L is the inductance dependent on the rotor position and phase current,

i is the phase current, and

ω_m is the rotor angular speed.

In Equation (2.1), the three terms on the right-hand side represent the resistive voltage drop, inductive voltage drop, and induced emf, respectively.

From the voltage equation, the equivalent circuit for one phase of the SRM is derived and shown in Fig. 2.3.
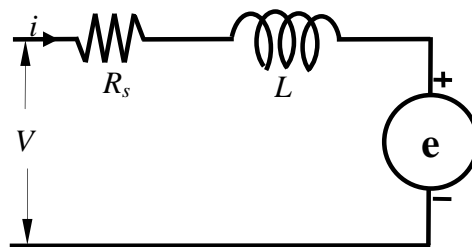
Fig. 2.3 Single-phase equivalent circuit of the SRM.

16

2.4 Analysis of torque production

2.4.1 Linear Analysis of Torque Production

Linear analysis assumes that there is no magnetic saturation and mutual inductance, and that all the flux cross the air-gap is in the radial direction. Based on Equation (2.1), the instantaneous electrical power is:

$$vi = R_s i^2 + Li\frac{di}{dt} + \omega_m i^2 \frac{dL(\theta, i)}{d\theta} \tag{2.2}$$

The energy stored in the magnetic field of an inductor in a linear medium is given by

$$\begin{aligned} W_{magnetic} &= \frac{1}{2}i\varphi \\ &= \frac{Li^2}{2} \end{aligned} \tag{2.3}$$

According to the law of conservation of energy, in the electromechanical systems whose predominant energy-storage mechanism is in magnetic fields, the energy transfer is as:

$$\begin{pmatrix} Energy\,input \\ from\,electric \\ sources \end{pmatrix} = \begin{pmatrix} Mechanical \\ energy \\ output \end{pmatrix} + \begin{pmatrix} Energy \\ stored\,in \\ magnetic\,field \end{pmatrix} + \begin{pmatrix} Energy \\ converted \\ to\,heat \end{pmatrix} \tag{2.4}$$

Hence, the mechanical power output P_{phase} is as following:

$$\begin{aligned} P_{phase} &= vi - R_s i^2 - \frac{dW_{magnetic}}{dt} \\ &= \omega_m i^2 \frac{dL}{d\theta} - \frac{1}{2}i^2 \frac{dL}{dt} \\ &= \omega_m i^2 \frac{dL}{d\theta} - \frac{1}{2}i^2 \frac{dL}{(\omega_m / d\theta)} \\ &= \frac{1}{2}\omega_m i^2 \frac{dL}{d\theta} \end{aligned} \tag{2.5}$$

17

The general expression for the torque produced by one phase at any rotor position can be expressed as

$$T_{phase} = \frac{p_{phase}}{\omega_m}$$
$$= \frac{1}{2}i^2\frac{dL}{d\theta}$$

(2.6)

Total instantaneous torque is given by the sum of the individual phase torques:

$$T_{total}(\theta, i_{ph}) = \sum_{phases} T_{phzse}(\theta, i_{ph})$$

(2.7)

2.4.2 Nonlinear Analysis of Torque Production

In an SRM, the magnetic saturation cannot be neglected; a nonlinear analysis is needed to take account of the saturation of the magnetic circuit [39]. The nonlinear analysis of the torque production is based on the magnetization curves shown in Fig. 2.4, which are a group of curves of flux-linkage φ as a function of excitation current i at a particular rotor position. It can be seen from Fig. 2.4 that the flux-current characteristics in the unaligned position are approximately linear because the magnetic path is dominated by large air-gap and flux densities are small. However, in the aligned position, the air-gap reluctance is small and flux density is high which cause high saturation at higher excitation currents.
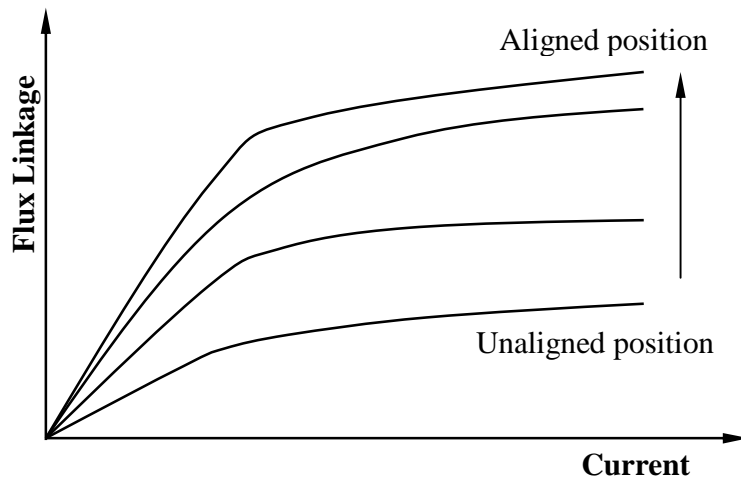
Fig. 2.4 Flux linkage, current and rotor position relationship.

18

Based on the electromechanical energy conversion theory, when a constant-current is supplied, the produced torque is equal to the mechanical work done W' during a rotor displacement $\Delta\theta$ divided by $\Delta\theta$, and this torque can be expressed as:

$$T_{phase} = \left[\frac{\partial W'}{\partial \theta} \right]_{i_{ph}=const} \tag{2.8}$$

During a typical motoring stroke, the locus of the operating point follows a curve similar to the one in Fig. 2.5, which is drawn together with the aligned and unaligned magnetization curves and the magnetization curve at the commutation position C. At point C, the supply voltage is reversed and the current freewheels through the diode. The mechanical work W_m is done between turn-on and commutation (suppose the phase was turned on at unaligned position), W_f is the work done after commutation. For the whole stroke, the power efficiency of SRMs can be defined as [5]:

$$\eta = \frac{W_f + W_m}{W_f + W_m + W_r} \tag{2.9}$$

where W_r is the energy returned to the source by using a regenerative converter.
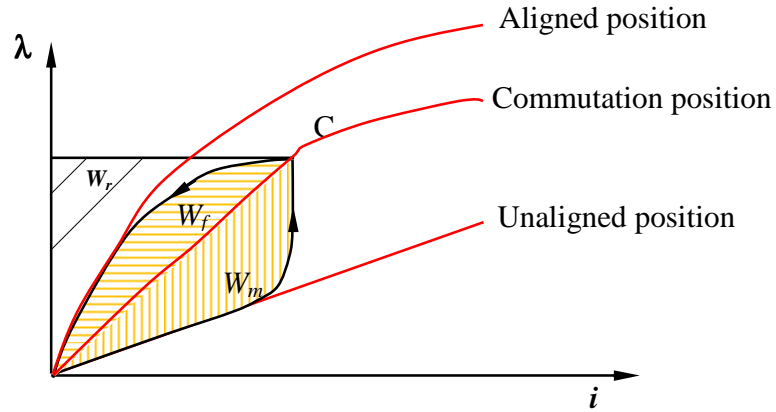
Fig. 2.5 Energy partitioning during one complete working stroke.

2.5 Four-quadrant Operation

According to [39], we assume that the positive rotation is in the counter-clockwise direction and the coil carries a constant current. At unaligned position, the leading edge of the rotor pole is aligned with the first edge of a stator pole; at aligned position, the rotor and stator poles are fully aligned.

When the rotor approaches the aligned position from unaligned position while the inductance is increasing, as shown in Fig. 2.6, positive torque is produced which means that the motor is in motoring mode. The torque changes direction at the aligned position. If the rotor continues past the aligned position with constant current in the stator, the attractive force between the poles produces a braking torque, which means that the motor is running in generating mode.

To keep the motor running in motoring mode, the phase current must be switched off while the stator and rotor poles are separating as shown in Fig. 2.7. The ideal current waveform is therefore a series of pulses synchronized with the rising inductance intervals. The ideal torque waveform has the same waveform as the current.
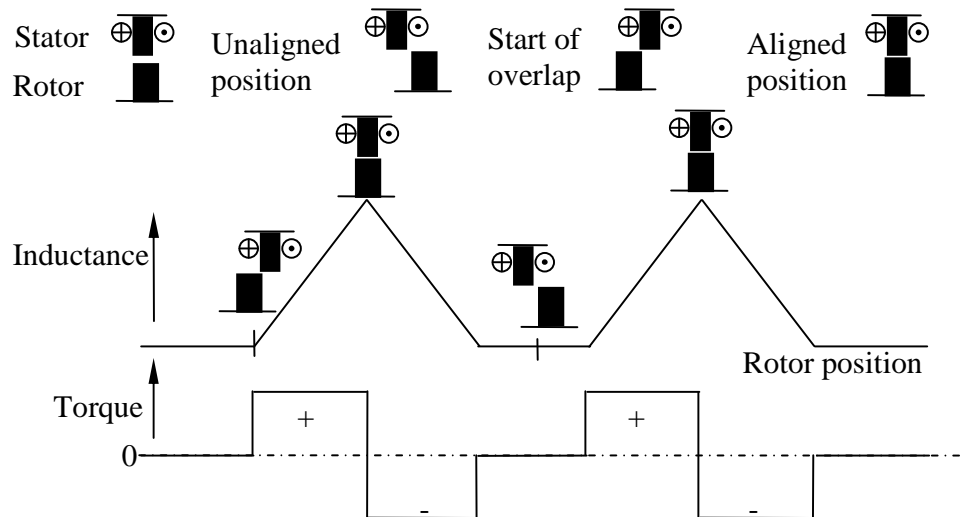
Fig. 2.6 Variation of inductance and torque with rotor position under constant phase current.
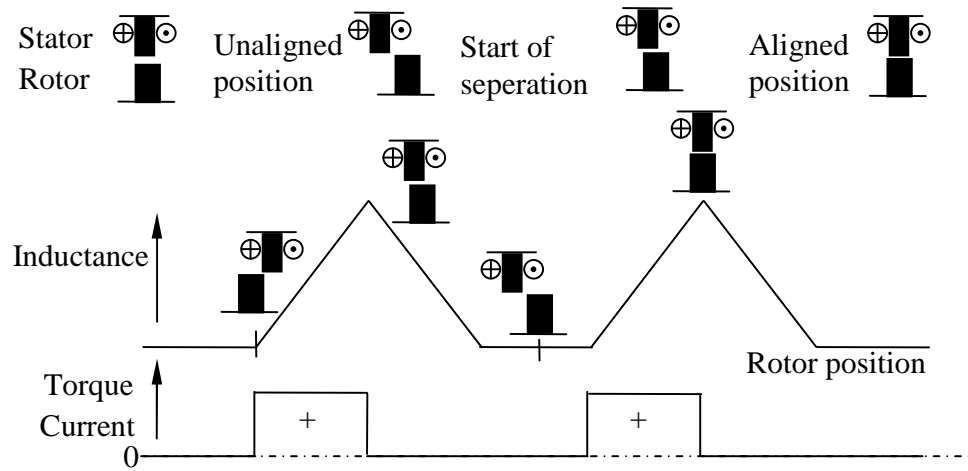
Fig. 2.7 Variation of inductance and torque with rotor position under ideal pulsed unidirectional current.

2.6 Torque-speed Characteristics

The torque-speed plane of an SRM drive can be divided into three regions [5], as shown in Fig. 2.8. The characteristics in these three regions are as following:

Region1: The constant torque limit region is the region below the base speed ω_b, which is the lowest possible speed for the motor to operate at its rated power. For the small back-emf in this region, the current can be set at any desired level by means of regulators such as hysteresis controller or voltage PWM controller.

Region2: The constant power limit region is the region where the controller maintains the torque inversely proportional to the speed. In this region, the phase excitation time falls off inversely with speed. Because torque is roughly proportional to the square of the current, the rapid decrease in torque with speed can be countered by adjusting the conduction angle θ_{dwell}. By advancing the turn-on angle to increase the conduction angle until it reaches its upper limit at speed ω_p, the phase current can be increased effectively to maintain the torque production at a high level.

Region 3: In this region, the θ_{dwell} upper limit is reached when it occupies half the electrical cycle. The torque in this region is governed by natural characteristics, falling off as $1/\omega^2$.
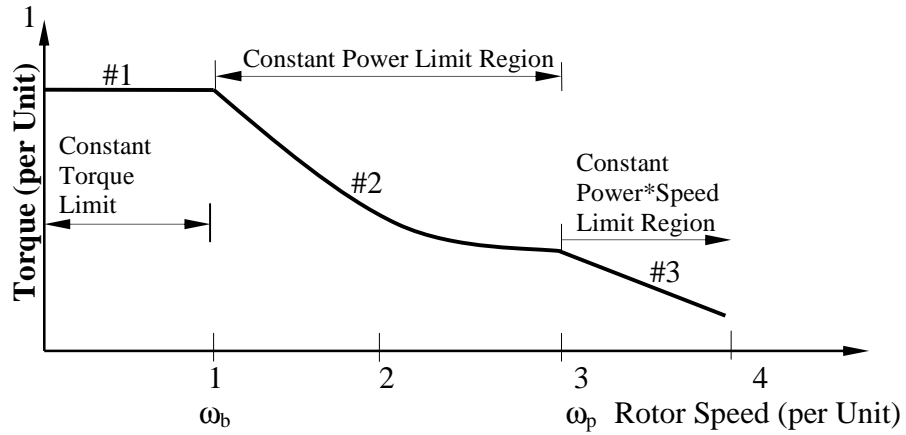
Fig. 2.8 Torque-speed characteristic of an SRM drive.

2.7 Loss Analysis of SRM

2.7.1 Stator Copper Loss

The stator copper loss at any time is the sum of the copper losses contributed by the instantaneous phase currents, which can be evaluated as follows [37]:

$$p_{cu} = i^2 R_s \left[1 + \frac{1}{12\pi} \left(T_r + T_f \right) \omega_m N_s N_r \right] \tag{2.10}$$

where i is the peak value of phase current,

T_r and T_f are the current rise and fall time,

N_s and N_r are the number of stator poles and rotor poles, and

The copper loss is dependent on speed. Therefore, it has to be considered only at the highest machine speed [40].

2.7.2 Core Loss

The core loss is difficult to predict in the SRM due to the variation of flux densities with time in stator segments. The core loss in an SRM consists of hysteresis and eddy current losses. Hysteresis loss is a heat loss caused by the magnetic properties of the armature. When an armature core is in a magnetic field, the magnetic particles of the core tend to line up with the magnetic field. When the armature core is rotating, its magnetic field keeps changing direction. The continuous movement of the magnetic particles, as

they try to align themselves with the magnetic field, produces molecular friction. This, in turn, produces heat.

Since iron is a conductor, a changing flux induces voltage and hence current, called eddy current, which circulates within the iron mass. These eddy currents produce losses, heat and demagnetization. To reduce the eddy current losses, the stator and rotor cores are laminated (built up from thin sheets electrically insulated from one another). The core losses can be calculated by using the Steinmetz equation [40]:

$$P_{fe\_loss} = C_h f B_{pk}^{a+bB_{pk}} + C_e f^2 B_{pk}^2 \qquad (2.11)$$

where C_h and C_e are the coefficients of hysteresis and eddy-current loss,

B_{pk} is the maximum flux-density,

f is the frequency, and

a and b are constants.

Manufacturers' loss data are usually presented in the form of graphs showing the total core loss as a function of frequency and flux density. In very high-speed applications, the core losses grow rapidly and may become the dominant component of losses.

2.8 Torque Control of SRM

Torque in the SRM is produced by pulses of phase currents synchronized with rotor position. The timing and regulation of these current pulses are controlled by the drive circuit and the torque control scheme. Usually there is no torque sensor and therefore the torque control loop is not a closed loop. Consequently, if smooth torque is required, any variation in the torque/current or torque/position relationships must be compensated in the feed-forward torque control algorithm, which implies that the torque control algorithm must be specifically programmed for a particular motor and possibly also for a particular application.

Generally, SRM can be operated from a voltage source or current source, which implies that the torque control of SRM can be either current control or voltage control. When operating from a voltage source, the controlled parameters can be the terminal voltage of the motor and the switching angles, and the voltage control can be achieved by

using a variable dc supply or modulating the bus voltage by using the switching devices. On the other hand, when operating from a current source, the controlled parameters can be the winding current of the motor and the switching angles, and the current control can be achieved by chopping.

2.8.1 Current Based Torque Control

Current controller takes the phase torque commands and generates the phase winding current commands as a function of rotor position. The principle of a current control method is shown in Fig. 2.9, in which phase inductance L_a, phase current command i_a^*, phase current i_a, terminal voltage V_a, and flux density B_a are displayed. Basically, the current controller starts to increase the phase current at the moment when the phase inductance increases, then maintains the current value within hysteresis value and cuts the current just before the inductance reaches its peak value. The positive and reverse voltage modes shown as V_a are used to make the winding current in square waveform.
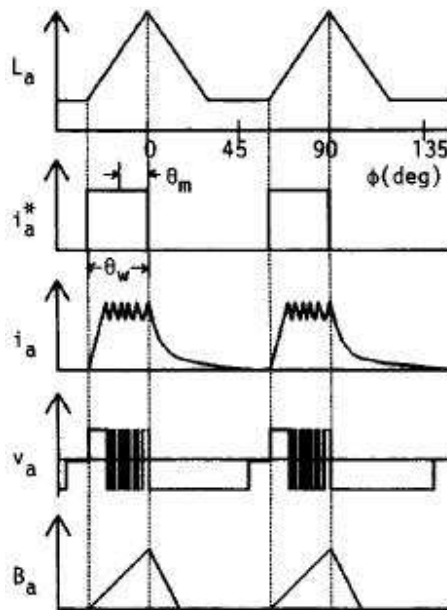
Fig. 2.9 Principles of current control method [41].

24

The diagram of a current-controlled SRM drive is shown in Fig. 2.10. The torque command is executed by regulating the current in the inner loop. The reference current i_a^* of a given operating point is determined from the load characteristics, the speed and the control strategy. A wide-bandwidth current transducer provides the current feedback information to the controller from each of the motor phases. The electronic commutator selects the appropriate phase for current regulation based on the instantaneous rotor position. The current controller generates the gating signal for the phases based on the information coming from the electronic commutator and the reference current command. The current in the commutated phase is quickly brought down to zero by applying negative V_a while incoming phase assumes the responsibility of torque production based on the commanded current.

Current controlled SRM drive can generate higher output power and higher output torque at low speeds [41]. When the drive is running at low speeds, by adjusting the current profile, it is possible to generate constant torque. And also by phase overlap excitation, the drive can produce higher torque and minimum torque ripple. Current controlled SRM drive also provides fast motor response [5].

However, when the flux density is high in the current controlled SRM drive, the efficiency is relatively low and iron loss is higher at low speeds. As the torque ripple is very sensitive to the current profiles [42], a slight deviation from the required profile, especially near the commutation region, produces high torque ripple. To get the current profile which can generate constant torque, this kind of drive requires high resolution position sensor and each phase current needs to be sensed.
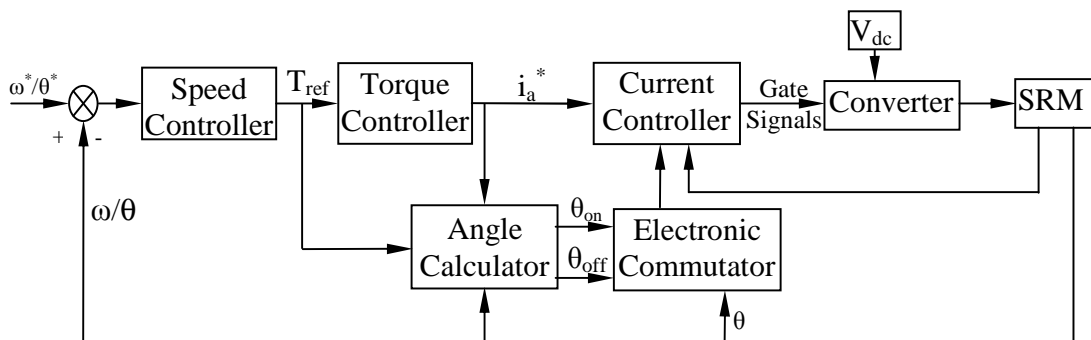
Fig. 2.10 Block diagram of current controlled SRM drive.

2.8.2 Voltage-based Torque Control

The voltage control method regulates terminal voltage of switched reluctance motors instead of winding current. The principle of voltage control is shown in Fig. 2.11, in which the phase inductance L_a, voltage command V_a*, terminal voltage V_a, winding current i_a, and flux density B_a are displayed. Basically, the voltage controller starts to apply the terminal voltage at the moment when the flux density increases, then maintain the terminal voltage value within hysteresis value and cut the voltage just before the flux density reaches its peak value. By adjusting the pulse width θ_w of PWM controller, the terminal voltage waveform can be kept in square shape. The advanced angle θ_m can be adjusted to give the best efficiency when the motor runs at different speeds. The reverse voltage is used to quickly bring down the flux density to zero. Unlike the current-controlled mode, the phase current here is not in square waveform.

The diagram of a voltage-controlled SRM drive is shown in Fig. 2.12. The torque command is executed by regulating the terminal voltage in the inner loop. The voltage command V_a^* of a given operating point is determined from the load characteristics, the speed and the control strategy, which is then compared with triangular PWM signals to generate the PWM pulses. The duty cycle of the PWM controller is adjusted according to the voltage command signal. The angle calculator is used to generate the turn-on and turn-off angles for a phase, depending on the rotor speed. The electronic commutator then generates the gating signals based on the control inputs, the instantaneous rotor position, turn-on and turn-off angles. The converter is driven by these pulses using positive or free-wheel mode.
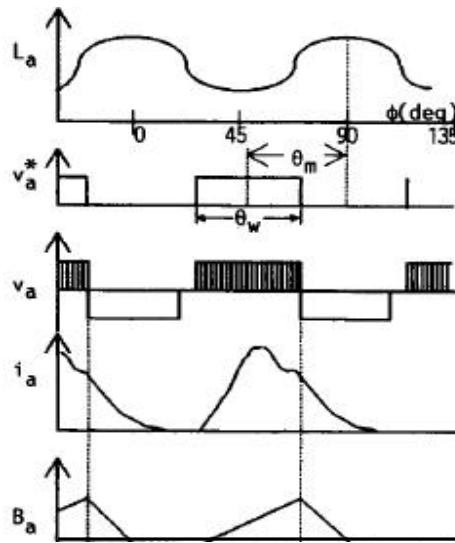
Fig. 2.11 Voltage control method [41].
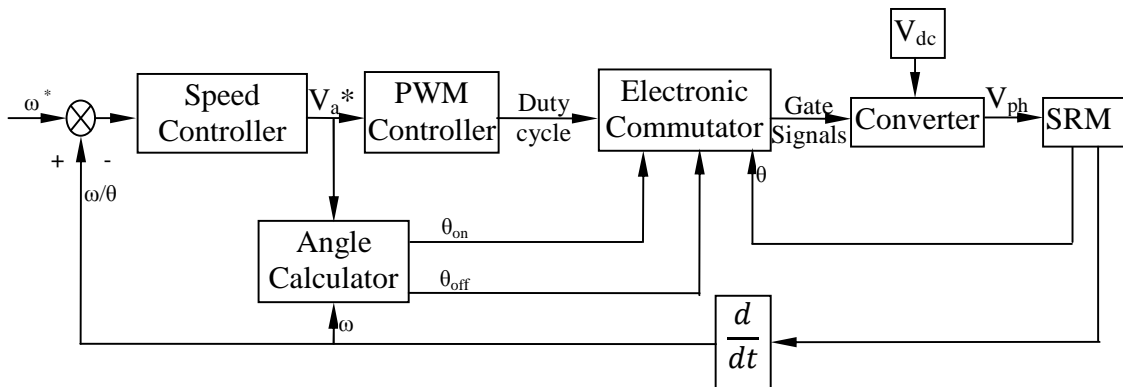
Fig. 2.12 Block diagram of voltage controlled SRM drive.

Compared with current-controlled SRM drive, the voltage controlled SRM drive has following advantages:

1. When using constant-frequency pulse width modulation (PWM), computational and memory requirements of this voltage-based control strategy are low.

2. SRMs also generate significantly lower noise when operating under voltage control rather than current control [43].

3. The voltage control is better in efficiency at high speed operations [41].

4. Voltage controlled SRM drive is generally less expensive, for it normally only uses one current-sensor in the DC-link for over-current protection and enables the use of a low resolution rotor position sensing system and reduces the signal processing requirement [44].

A voltage controlled SRM drive, however, is more sensitive to voltage ripple on the power bus and has a lower control bandwidth. Due to the skipping cycles during voltage PWM regulation, the SRM drive exhibits the abnormal periodic behavior, in which the distributions of both current and torque are severely uneven [45].

2.8.3 Comparison

Based on the previous analysis, four factors emphasized in most applications are summarized in Table 2.2.

Voltage control is attractive for low-power/low-cost SRM drives due to the reduced number of current sensors and signal processing requirement. When minimum torque ripple and fast response required from the drive, current control should be applied. In high speed range, voltage control should be considered when high efficiency is the main concern.

For the HEV application, when the vehicle is running at low or medium speeds, the torque ripple should be taken into consideration, so the current control is more suitable. But when the motor is running at high speeds, the large inertia of the vehicle can effectively smooth out the torque ripple of the SRM and the motor efficiency becomes the most important performance criterion of the vehicle drive-train, the torque control method should be changed to voltage-based control, which can be applied by advancing the turn-on angle and adjusting the conduction angle.

Table 2-2 Comparison of torque control methods

Control method	Cost	Simplicity	Percentage of torque ripple	efficiency
Current-based torque control	high	complex	low	low
Voltage-based torque control	low	simple	high	high

3   BACK-PROPAGATION ARTIFICAIL NEURAL NETWORK

3.1   History of Artificial Neural Network

Artificial neural networks (ANNs) or just neural networks (NNs) are information processing systems that roughly mimic the behaviour of a human brain by emulating the operations and connectivity of biological neurons [46]. NNs consist of a large number of simple processing elements called neuron, which has an internal state called activation function. Each neuron is connected to other neurons with an associated weight. Hence, the NN can be characterized by (1) architecture which is the pattern of connections between neurons, (2) training algorithm which is used to determine the weights on the connections, and (3) activation functions of the neurons. NNs can be trained directly from data, sometimes complicated or imprecise data, which means that NNs are applicable to patterns extracting and trends detecting, nonlinear functional mapping and controlling, pattern recognition and data classification, image processing and signal processing.

The development of the NNs stemmed from the 1940s, and motivated by a desire to try to understand the brain and to emulate some of its strengths. An important step toward artificial neural networks occurred in 1943 when Warren McCulloch and Walter Pitts wrote a paper on the working mechanism of the neurons and modeled a simple neural network with logic circuits [47]. However, the first significant application only took place in 1958 when Rosenblatt introduced a large class of ANNs called perceptrons which typically consisted of an input layer connected by paths with fixed weights to associate neurons [48]. In 1960, Bernard Widrow and Marcian Hoff developed models called ADALINE in electrical engineering for single-layer network and MADALINE for multilayer network [49].

Due to the limitation of single-layer perceptrons and the lack of a general training method for multilayer net, 1970s became the quiet years for the development of NNs. The renewed enthusiasm started in 1980s after Rummelhart and Mclelland introduced a general back-propagation algorithm for a multilayered perceptron (MLP) network in 1986 [50], [51]. The basic MLP-network is constructed by ordering the units in layers, letting each unit in a layer take an input only from the outputs of units in the previous

layer or eternal inputs. Hence, the MLP network is usually called a feed-forward network. If the MLP-network architecture is augmented with feedback loops, the network is usually referred to as a recurrent network. Another suitable network for modelling and control of dynamic system is the Radial Basis Function (RBF) network developed in 1992 by Sanner and Tzirkel-Hancock [52].
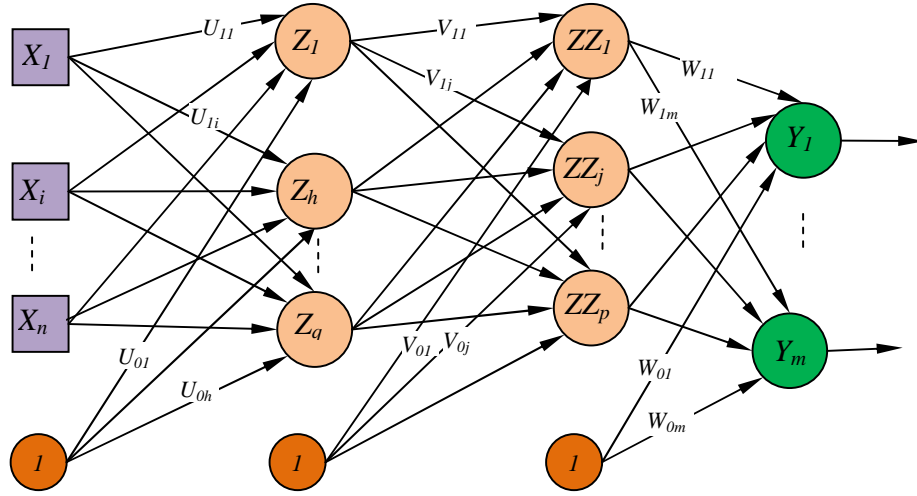
3.2 Back-propagation ANN

A back-propagation neural network is a multilayer feed-forward network trained by back-propagation algorithm. As is the case with most neural networks, the aim is to train the network to achieve a balance between the ability to respond correctly to the input patterns that are used for training (memorization) and give reasonable response to input that is similar to that used in training (generalization).

The training of a network by back-propagation involves three stages: the feed-forward of the input training pattern, the calculation and back-propagation of the associated error, and the adjustment of the weights. After training, application of the net involves only the computations of the feed-forward phase. Even if training is slow, a trained net can produce its output very rapidly. A multilayer net (with one or more hidden layers) can learn any continuous mapping to an arbitrary accuracy. For control application, single-hidden-layer networks are not sufficient for stabilization, especially in discontinuous mapping, two-hidden-layer networks are enough assuming that bias units are used.

3.2.1 Architecture

A back-propagation neural network with two hidden layers is shown in Fig. 3.1. Both the output units and the hidden units have biases. The bias on a typical output unit Y_k is denoted by W_{0k}; the bias on a typical hidden unit Z_j is denoted by U_{0h}, and the bias on a typical hidden unit ZZ_j is denoted by V_{0j}. These biases act like weights on connections from units whose output is always 1.

The weight linking a typical input unit X_i with the typical unit Z_h in the first hidden layer is denoted by U_{ih}; The weights linking a unit Z_h in the first hidden layer with a unit ZZ_j in the second hidden layer is denoted by V_{hj}; The weights linking a unit ZZ_j in the second hidden layer with a typical output unit Y_k is denoted by W_{jk}.

Fig. 3.1 Architectural graph of a BPNN with two hidden layers.

Each neuron has an activation function which can be sigmoid, bipolar sigmoid, log-sigmoid function, etc. The weights on connections can be determined by the back-propagation algorithm during training process, and then used for calculating the outputs. For some applications, these weights can be used to initialize the neural network and then updated by using online training algorithm.

3.2.2 Training with Levenberg–Marquardt Algorithm

The process of changing weights is called training, which minimizes the error caused by the difference between desired output and actual output. There are several commonly used training methods for BPNN such as gradient descent, Gauss-Newton algorithm (GNA) and Levenberg-Marquardt algorithm (LMA). The LMA has been a compromise between the GNA and the method of gradient descent, which is more robust but slower than the GNA, and faster but less stable than the gradient descent.

To train the BPNN, generally, the performance index $F(w)$ to be minimized is defined as the sum of squared errors between the target outputs and the network's response outputs, namely

$$F(W) = e^T e \tag{3.1}$$

where $W=[U_{01}, ..., U_{np}, V_{01}, ..., V_{qp}, W_{01}, ..., W_{pm}]^T$ consists of all weights of the network, e is the error vector comprising the errors between the responses and the targets.

The training using LMA is an iterative procedure to find the suitable weights vector to minimize the performance index. The standard LMA training process can be illustrated as following:

3.2.2.1 Feed-forward

During feed-forward, each input unit receives an input signal and broadcasts it to each of the hidden units in the first layer. Each of these hidden units then computes its activation and sends its output to the hidden units in the second layer. Next, each hidden unit in the second layer computes its activation and sends its output to the output units. Finally, each output unit computes its activation to form the response of the net for the given input pattern and calculate the error between the response and the actual output. The detailed description is like the following [46]:

Each input unit (X_i, $i=1, ..., n$)

    1) broadcasts the input signals to hidden units in the first hidden layer.

Each hidden unit (Z_h, $h=1, ..., q$) in the first hidden layer

    1) computes the input signal

$$z\_in_h = U_{0h} + \sum_{i=1}^{n} X_i U_{ih} \qquad (3.2)$$

    2) applies activation function to compute the output signal

$$Z_h = f(z\_in_h) \qquad (3.3)$$

    3) and sends its output signal to the units in the second hidden layer.

Each hidden unit (ZZ_j, $j=1, ..., p$) in the second hidden layer

    1) computes the input signal

$$zz\_in_j = V_{0j} + \sum_{h=1}^{p} Z_h V_{hj} \qquad (3.4)$$

    2) applies activation function to compute the output signal

$$ZZ_j = f(zz\_in_{j)} \qquad (3.5)$$

    3) and sends its output to the output layer.

Each output unit (Y_k, $k=1, ..., m$)

    1) sums weighted input signal

$$y\_in_k = W_{0k} + \sum_{j=1}^{p} ZZ_j W_{jk}$$
(3.6)

    2) applies activation function to compute the output signal

$$Y_k = f(y\_in_k)$$
(3.7)

    3) and calculates the error

$$e_k = T_k - Y_k$$
(3.8)

where $e=\{e_k\}_{k=1,...,m}$,

    T_k is the target, and

    Y_k is the corresponding response output.

3.2.2.2 *Backpropagation of Error*

The difference between different training algorithms is the way to get the increment of the weights vector W which includes all the weights between the neurons. When training with the LMA, the increment of weights ΔW can be obtained as follows

$$\Delta W = \left[J^T J + \lambda diag(J^T J) \right]^{-1} J^T e$$
(3.9)

where J is the Jacobian matrix whose i^{th} row equals to

$$J_i = \frac{\partial F(X_i, W)}{\partial W}$$
(3.10)

which is the gradient of the performance index $F(W)$ with respect to the weight and bias variables,

    λ is the training parameter which is to be updated using the decay rate β depending on the outcome. In particular, λ is multiplied by the decay rate β ($0< \beta < 1$, $\beta=0.1$ by default in MATLAB) whenever $F(W)$ decreases, while λ is divided by β whenever $F(W)$ increases in a new step.

3.2.2.3 Update Weights and Biases

The weights for all layers are adjusting simultaneously to speed up the training process [46]:

For each output unit ($j = 0, ..., p; k = 1, ..., m$):

$$w_{jk}(new) = w_{jk}(old) + \Delta w_{jk} \tag{3.11}$$

For each hidden unit ZZ_j ($h = 0, ..., q; j = 1, ..., p$):

$$v_{hj}(new) = v_{hj}(old) + \Delta v_{hj} \tag{3.12}$$

For each hidden unit Z_h ($i = 0, ..., n; h = 1, ..., q$):

$$u_{ih}(new) = u_{ih}(old) + \Delta u_{ih} \tag{3.13}$$

Finally, test the stopping condition. If the performance index is less than the desired value, training is stopped and the weights are fixed for application, or else do steps described from 3.2.2.1 to 3.2.2.3.

3.2.3 Activation Function

An activation function for a back-propagation network should have several important characteristics such as: continuous, differentiable, and monotonically non-decreasing. Furthermore, for computational efficiency, it is desirable that its derivative should be easy to compute. Usually, the function is expected to saturate, i.e., approach finite maximum and minimum values asymptotically. The three functions used in this research are: tansig(), logsig(), and purelin(), which are shown in Figs. 3.2 to Fig. 3.4.

$$tan\,sig(\,n\,) = \frac{2}{1 + e^{-2n}} - 1 \tag{3.14}$$

y=tansig(n)
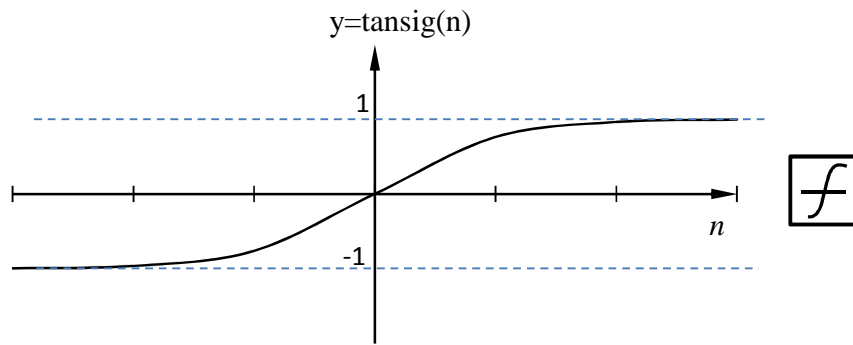
Fig. 3.2 Bipolar sigmoid, range (-1, 1).

$$\log sig(n) = \frac{1}{1 + e^{-n}}$$ (3.15)

y=logsig(n)
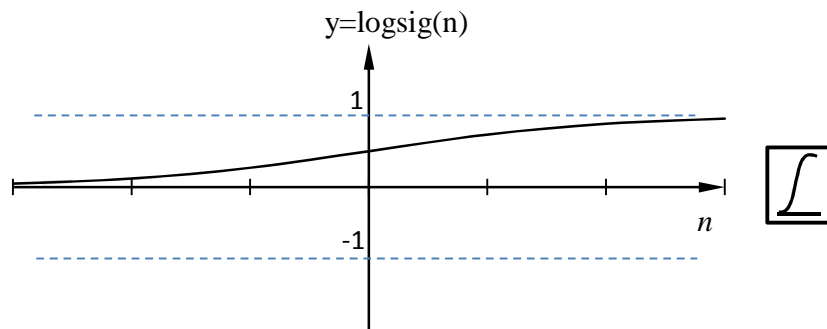
Fig. 3.3 Binary sigmoid, range (0, 1).

$$purelin(n) = n$$ (3.16)

y=puresig(n)

Fig. 3.4 Linear transfer function.

3.2.4 Number of Hidden Layers

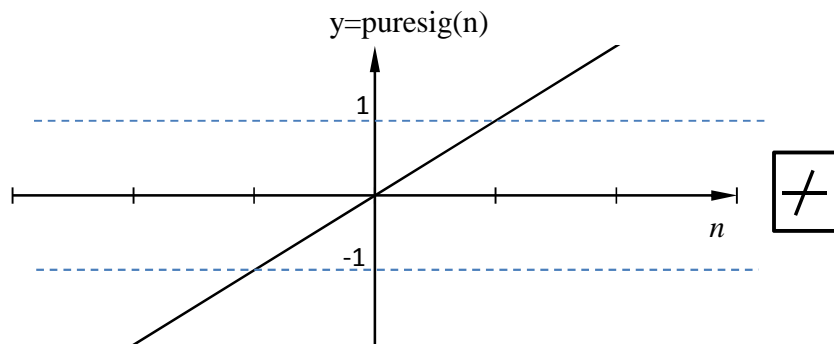A multilayer net (with one or more hidden layers) can learn any continuous mapping to an arbitrary accuracy. However, for control application, single-hidden-layer networks are not sufficient for stabilization, especially in discontinuous mapping, two-hidden-layer networks are enough assuming that bias units are used [53].

3.2.5 Application Procedure

After training, for a fixed weight BPNN, it is applied by using only the feed-forward phase of the training algorithm. The application procedure is as following:

(1) Initialize weights obtained from the training algorithm

(2) For each input vector,

Each input unit (X_i, $i=1, \ldots, n$),

broadcasts input signal to hidden units.

Each hidden unit (Z_h, $h=1, \ldots, q$)

$$z\_in_h = U_{0h} + \sum_{i=1}^{n} X_i U_{ih} \tag{3.17}$$

$$Z_h = f(z\_in_h) \tag{3.18}$$

Each hidden unit (ZZ_j, $j=1, \ldots, p$)

$$zz\_in_j = V_{0j} + \sum_{h=1}^{p} Z_h V_{hj} \tag{3.19}$$

$$ZZ_j = f(zz\_in_j) \tag{3.20}$$

Each output unit (Y_k, $k=1, \ldots, m$)

$$y\_in_k = W_{0k} + \sum_{j=1}^{p} ZZ_j W_{jk} \tag{3.21}$$

$$Y_k = f(y\_in_k) \tag{3.22}$$

### 3.2.6 Direct Inverse Neural Network Based Control

For nonlinear systems, since it cannot be described in terms of transfer functions, it is often seen that neural networks are proposed as a tool for adaptive control of nonlinear systems with time-varying dynamics due to its high learning and generalization ability [54]. There are different models for neural-network based control such as direct

inverse control, internal model control and nonlinear predictive control, however, due to requisite for good dynamic performance and cost sensitivity of the HEVs traction application, in this research, direct inverse control is selected for it is simple to implement and fast response ability. For direct inverse control, the controller is inferred directly from a set of data without requiring an actual mathematical model of the system.

Direct inverse control utilises an inverse system model [55]. Fig. 3.5 shows the principle of training the inverse system model. With the input signal S, the plant output Y is used as input to the neural network. The network calculated the output Y' and then compared it with the training signal (the system input S) and this error is used to train the network to update the weights. With extensive training, this structure will clearly tend to force the network to represent the inverse of the plant.

Then, the inverse system model is connected with the plant to implement control function as shown in Fig. 3.6. During real-time control, for a certain output command, the NN inverse model can produce the input for the plant which will drive the plant tracking the output command.
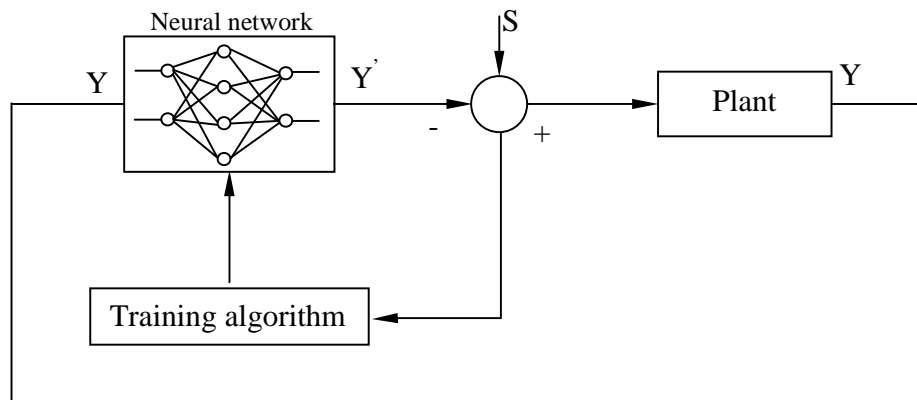
Fig. 3.5 Training of direct inverse model.
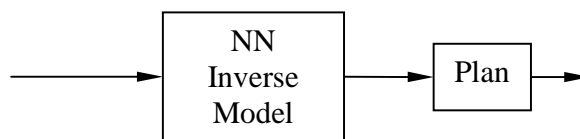
Fig. 3.6 Principle of direct inverse control.

The drawback of this approach is that if the nonlinear system mapping is not one-one then an incorrect inverse model can be obtained. To address this problem, in this research, the training data have been divided into several contiguous data sets to train several neural networks to increase the accuracy of the inverse system mode.

# 4 TORQUE RIPPLE MINIMIZED TORQUE CONTROL OF SRM

4.1 Introduction

In an HEV, the on-board electric motor serves as a device to optimize the efficiency of the internal combustion engine (ICE). HEVs typically employ permanent-magnet synchronous motor. Recently, switched reluctance motor (SRM) has attracted interest for HEV propulsion for its robust construction, fault tolerant operation, high starting torque without the problem of excessive inrush current, and ability to extremely high-speed operation. However, SRM suffers from some drawbacks such as high torque ripple and acoustic noise which are quite critical for HEV applications [5].

Due to considerable non-linearity in the torque characteristics of SRM, and the extensive requirement for lower torque ripple, good dynamic performance and cost sensitivity of the HEVs traction application, in this research, a feed-forward back propagation neural network (BPNN) based direct inverse control is proposed to minimize the torque ripple at low speeds for its simple, easy to implement and fast dynamics. Special data pre-processing technique has been used to handle the problem of multi-valuedness. By splitting the training data into several contiguous sets and designing a bank of two-hidden-layer neural network controllers for the whole torque range, the appropriate current profile to reduce the torque ripple is obtained. Computed results show that the proposed scheme can reduce the torque ripple and provide good dynamic performance with respect to changes in the torque commands.

4.2 Design of Neural Network Based Controller

4.2.1 Diagram of the Controller

The diagram of the proposed BPNN-based torque controller is shown in Fig. 4.1. The commutation logic selects the appropriate phases that can be conducted simultaneously to reduce the torque ripple based on the instantaneous rotor position. The torque distribution is used to calculate the phase torque commands by using torque distribution function discussed in [56]. Torque command, rotor position and outputs from the commutation logic are then used to generate phase torque command.
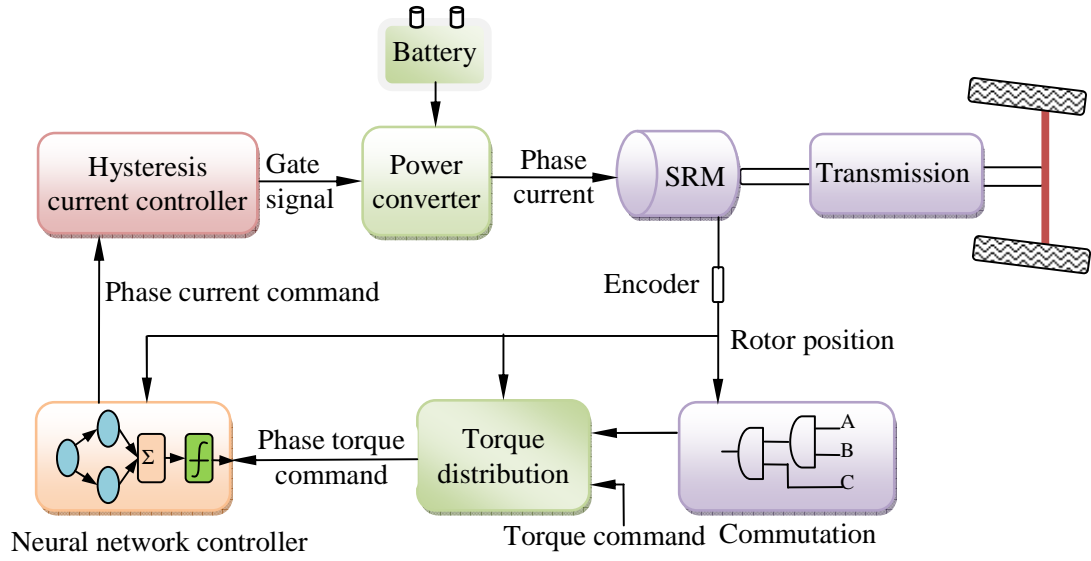
Fig. 4.1 Diagram of the proposed controller.

Neural network controller is then used to track the torque command. By taking reliability, speed and cost into consideration, BP neural network is applied to learn the phase current profile for the calculated phase torque command and to produce the phase current command. The hysteresis current controller has been chosen for its simplicity and robustness and an asymmetric H-bridge converter is applied to follow the current command for its simplicity and high stability.

4.2.2   Torque Distribution Function

At any time, the resultant output torque of SRM is the summation of the output torques in all phases:

$$T = \sum_{j=1}^{N} T_j \tag{4.1}$$

where N is the number of phases, and T_j is the torque generated in phase j which is a nonlinear function of phase current i and rotor position θ. Assuming that the rotor position is $0°$ or $60°$ (Mechanical degree) when fully aligned with the stator, for an 8/6 SRM, the position of the rotor when fully unaligned with the stator is $30°$. Neglecting the influence of saturation, if the phase current i is fixed, the torque (of an 8/6 SRM) will have a profile as shown in Fig. 4.2.
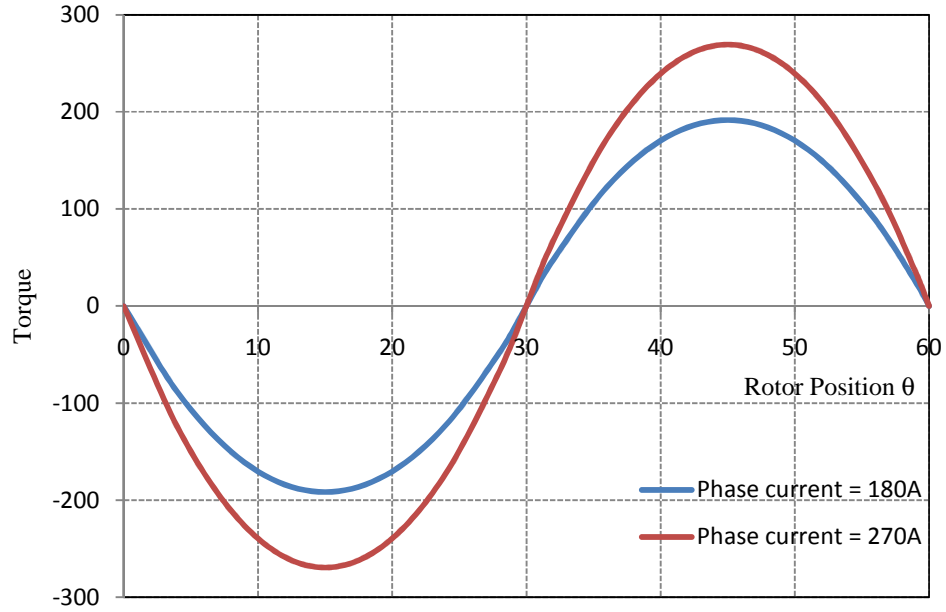
Fig. 4.2 Phase torque profile under fixed current.

It is clear that high torque is not available near fully aligned/unaligned position even when high phase current is presented. To generate a ripple-free output torque, there must be overlapping between phases.

During phase overlapping, the current is decreasing in one phase and increasing in the other phase. To obtain a constant torque, the sum of the torque generated by these two phases must be equal to the torque generated by one phase in non-overlapping period. To determine the desired torque produced by each phase, torque-factors have to be introduced, which are defined as

$$T = \sum_{i=1}^{N} f_i(\theta)T_{com} \qquad \textbf{(4.2)}$$

where $f_i(\theta)$ is the torque factor for phase i at rotor position θ, and T_{com} is the torque command.

The motor used in this research is an 8/6 SRM, the inductance increasing/decreasing period for each phase is $\pi/6$, the angle between the two adjacent stator phases is $\pi/4$. To generate desired torque ($T = T_{com}$), a conduction angle of $\pi/8$ is chosen in this research. This means,

$$\theta_{off} - \theta_{on} = \pi/8 \tag{4.3}$$

So the phase overlapping for the two adjacent phases is $\pi/8 - \pi/12 = \pi/24$. During phase overlapping, the torque factor for phase j is expressed as follows [56],

$$f_i(\theta) = \begin{cases} 0.5 - 0.5\cos(24*(\theta_i - \theta_{on})) & \theta_{on}\langle\theta \leq (\theta_{on} + \pi/24) \\ 1 & (\theta_{on} + \pi/24)\langle\theta \leq (\theta_{off} - \pi/24) \\ 0.5 + 0.5\cos(24*(\theta_i - \theta_{off} - \pi/24)) & (\theta_{off} - \pi/24)\langle\theta\langle\theta_{off} \\ 0 & other \end{cases} \tag{4.4}$$

and the torque command T_{ref} for the to-be-excited phase can be calculated as follows:

$$T_{ref} = f(\theta)*T_{com} \tag{4.5}$$

4.2.3 Neural Network Controller

The static torque characteristic for a single conducting motor phase of SRM is shown in Fig. 4.3 which shows a highly non-linear characteristic. SRM will produce different torque when the rotor is at different positions under a certain phase current excitation. Obviously, in an inverse model of SRM, there are many different input data pairs (torque, rotor position) that will be mapped to one output current which is called a multi-valued inverse mapping.
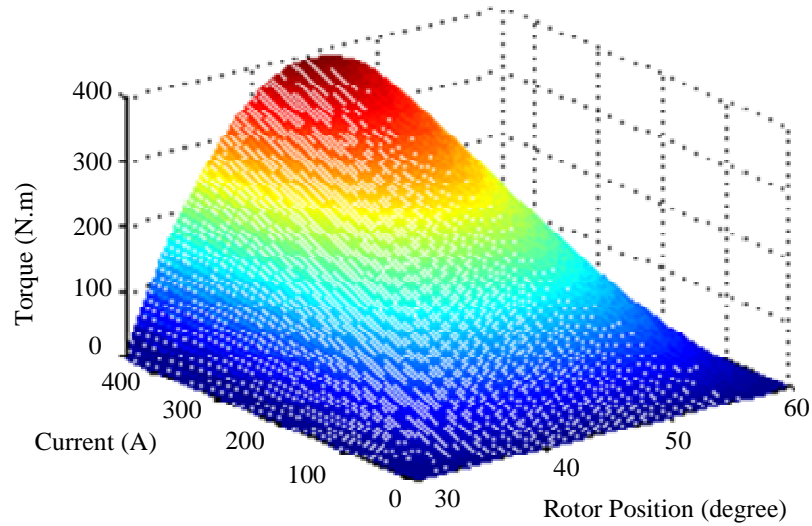

Fig. 4.3 Static torque characteristic for one phase.

42

Generally, for this kind of model, during training, the feed-forward network tends to average the weights corresponding to various inputs, thereby cannot produce a high accuracy mapping. After training, for a certain input pairs (torque, rotor position), an accurate current cannot be calculated from the inverse mapping. To make the inverse model learning the current profile properly, the training data have to be split into several data sets, and each data set is used to approximate one branch of the inverse model by using one neural network. Considering the complexity of a set of neural networks and the accuracy needed for torque tracking, the original data are analyzed and the redundant data are removed to get the final training data. The training data for the whole torque range are then divided into three data sets and used to train three neural networks.

As single-hidden-layer networks are not sufficient for stabilization, especially in discontinuous mapping, two-hidden-layer networks are enough assuming that bias units are used. In this work, for each neural network, a four-layer neural network comprising of an input layer, an output layer and two hidden layers is used. Levenberg-Marquard algorithm described in previous chapter has been chosen to train the feed-forward neural networks due to its fast training speed. The training data have been divided into validation set and test set to get good generalization.

One of the neural networks is shown in Fig. 4.4. The input layer has bias and two input units which are rotor position and phase torque command, the output layer has one output unit which is the phase current command. The activation functions for the hidden layers 1 and 2 are either hyperbolic tangent sigmoid function or log-sigmoid function, the output layer activation function is linear transfer function, and the learning function is gradient descent with momentum weight and bias learning function.
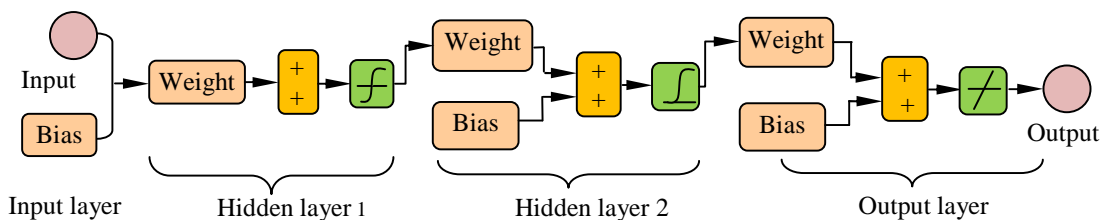
Fig. 4.4 Structure of one of the neural networks.

4.2.4 Hysteresis Current Control

From previous section, the reference phase current for each phase is determined by the desired torque and current rotor position through the neural network controller. Then hysteresis current control technique will be applied to maintain the phase current within an acceptable range around the reference phase current. The principle of the hysteresis current control is shown in Fig. 4.5.

As shown in Fig. 4.5, when the phase is excited, the output of PWM is 1, the power converter applies voltage to the phase. If the current reaches the upper limit, the output of PWM is changed to 0 which cuts off the supply voltage until the current reaches the lower limit. If the current reaches the lower limit, the output of PWM is changed to 1 which lets the power converter supply the voltage until the current reaches the upper limit. If the current is within the band Δh, the PWM output remains unchanged.

4.3 Simulation Results and Analysis

The proposed SRM torque controller has been simulated by using the motor described in Appendix A1 in Matlab/Simulink as shown in Fig. 4.6. Corresponding to different conditions in the propulsion, the performances of the SRM are calculated and analyzed when it is running at different conditions such as steady-state, dynamic state and starting from stand-still.
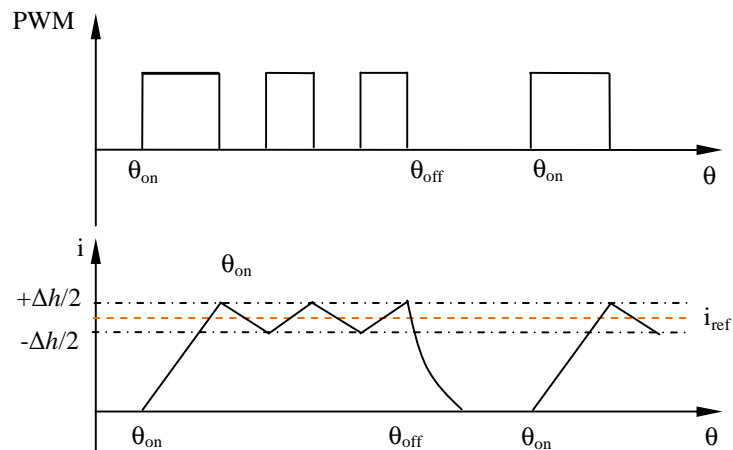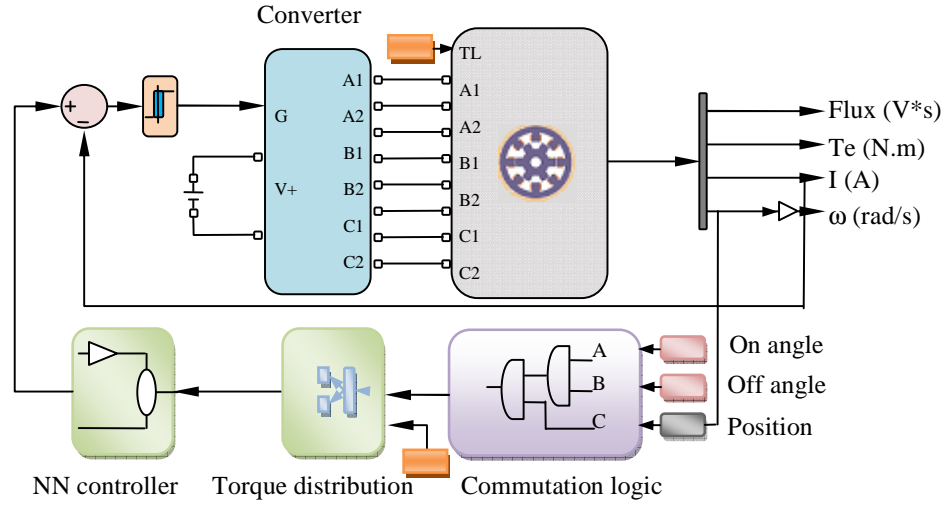

Fig. 4.5 Hysteresis current control and PWM output.

Fig. 4.6 Simulation model of NN torque controller.

4.3.1　Steady-State Performance

During most of the time, vehicle runs at steady-state under constant load. The vehicle control unit expects a precise and stationary average torque of the electric drive which can track precisely the reference torque.

To analyze the controller performance under steady-state, the torque command (T_{com}) was set to 350 N.m, the motor speed was 525 rpm, and the rotor inertia was set to a very high value to keep the vehicle speed constant. The 4-phase currents and torque output under this operating condition are shown in Figs. 4.7(a) and (b). Fig. 4.7(b) shows that the torque output (T_{out}) reaches 350.1 N.m in 0.0014 s and, after that, the output torque varies between a maximum torque (T_{max}) of 364.3 N.m and a minimum torque (T_{min}) of 336.5 N.m. The average torque output (T_{avg}) has been found to be 350.8 N.m. Using this information, the torque ripple in percentage can be calculated by employing (4.6) [57]

$$T_{ripple} = \left[(T_{\max} - T_{\min}) / T_{avg} \right] \times 100\% \tag{4.6}$$

which is 7.9%. This torque ripple is produced due to the discrepancy between the output current command of the neural network controller and the ideal current profile for the torque command. The second reason is due to the output current of the hysteresis current controller which is not exactly equal to the current command. It is also found that, during

the commutation period, the torque ripple is higher than that when only one phase is excited. The reason for this is that the total torque in the commutation period is the sum of the two individual phase torques, and the total torque ripple is therefore the sum of the two phase torque ripples which results in a higher torque ripple.
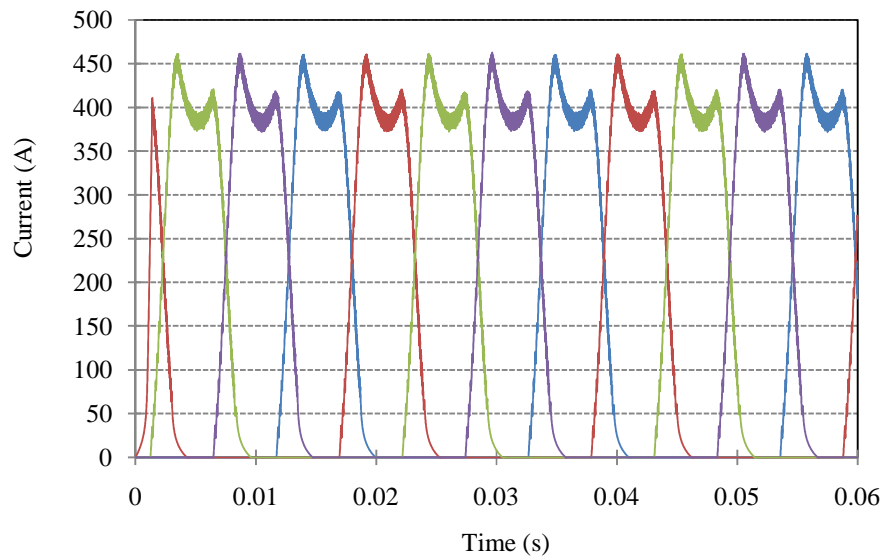

(a)
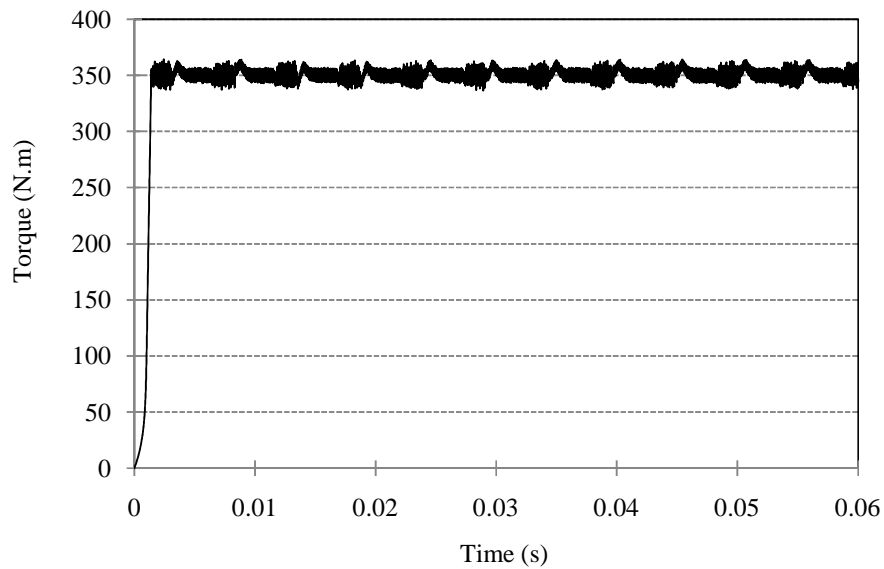
(b)

Fig. 4.7 Calculated waveforms at low speed (477.5 rpm) with a torque command of 350 N.m.
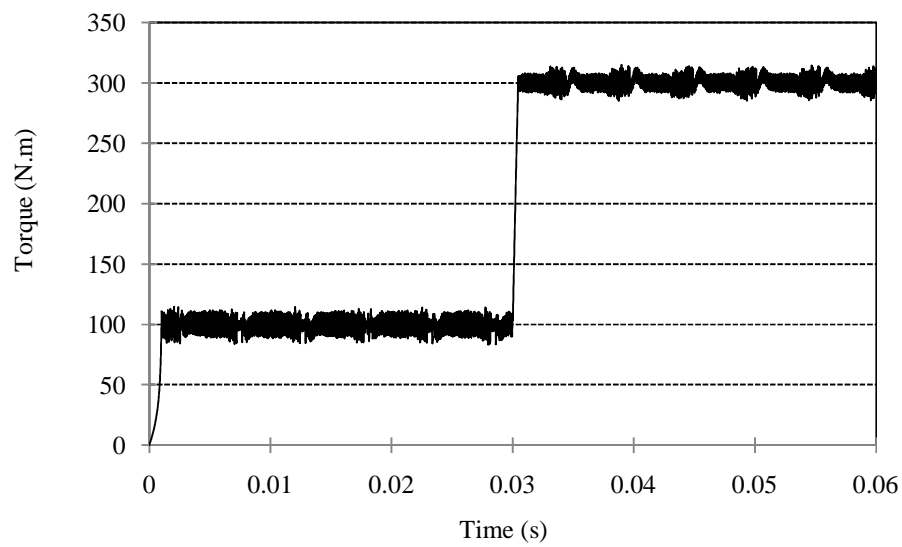**(a) 4-phase currents. (b) Output torque.**

4.3.2 Dynamic Performance

While the vehicle is running at constant speed like under cruise control, the load torque can vary abruptly due to the change of the road condition. When the vehicle is running at this kind of state, the control unit also expects a precise average torque and fast response from the electric drive.

In the dynamic performance simulations, the speed was also kept constant by using a high motor inertia. Two cases were considered: in the first case, as shown in Fig. 4.8, the command torque, T_{com}, was changed from 100 N.m to 300 N.m at 0.03 s and, in the second case, T_{com} was changed from 350 N.m to 300 N.m at 0.03 s as presented in Fig. 4.9. Fig. 4.8 (b) shows that the dynamic performance of the controller is very good; T_{out} increases to 300.2 N.m at 0.0304 s. Fig. 4.9 shows the calculated 4-phase currents and output torque of the SRM when T_{com} was reduced from 350 N.m to 300 N.m at 0.03 s. The motor drive responds almost instantaneously as shown in this figure, T_{out} reaches 300 N.m at 0.0301 s. T_{avg}, T_{min} and T_{max} are 301.4 N.m, 284.4 N.m, and 317.8 N.m respectively. By using (4.6), the average torque ripple has been found to be 11%. The reason for this is similar to that for the steady state.
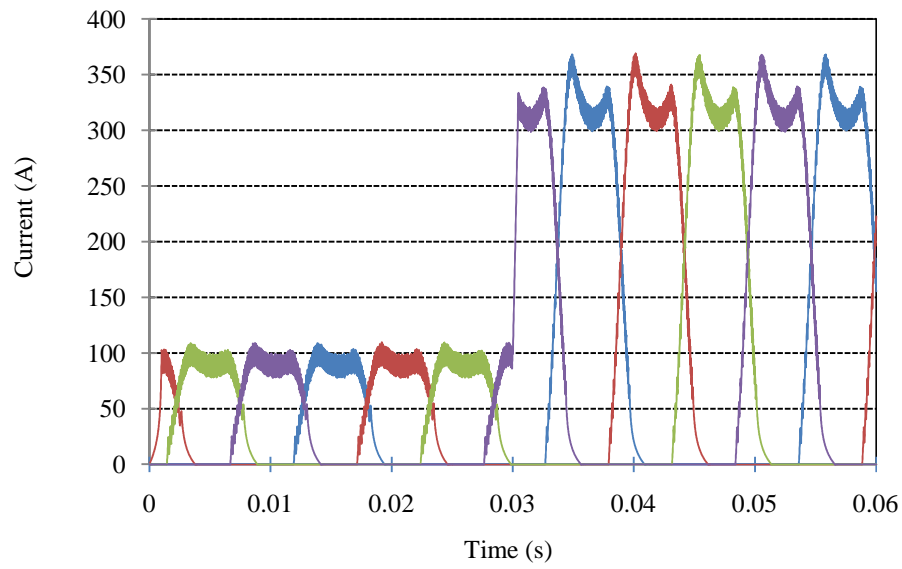
(a)

(b)

Fig. 4.8 Calculated waveforms at speed of 477.5 rpm with an initial torque command of 100 N.m changed to 300 N.m at 0.03 s.
(a) 4-phase currents. (b) Output torque.
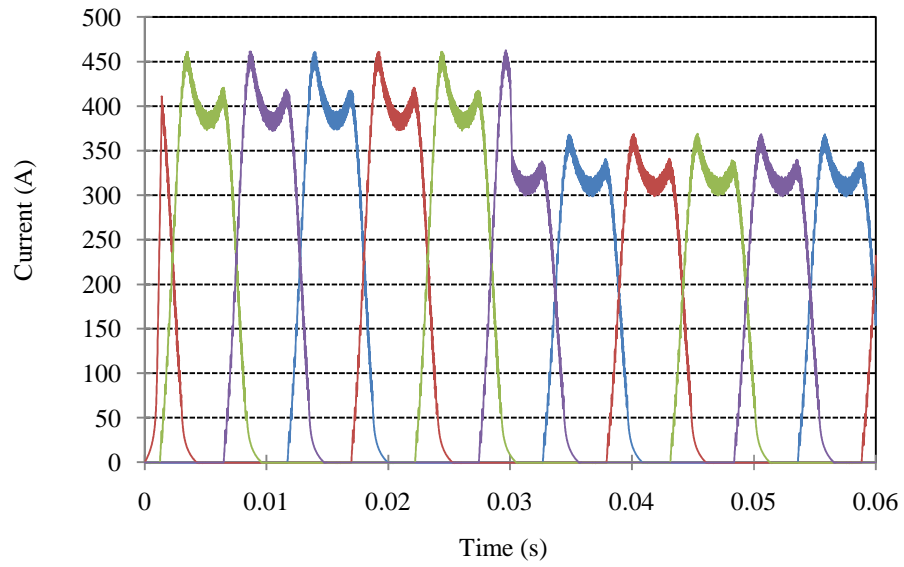
(a)
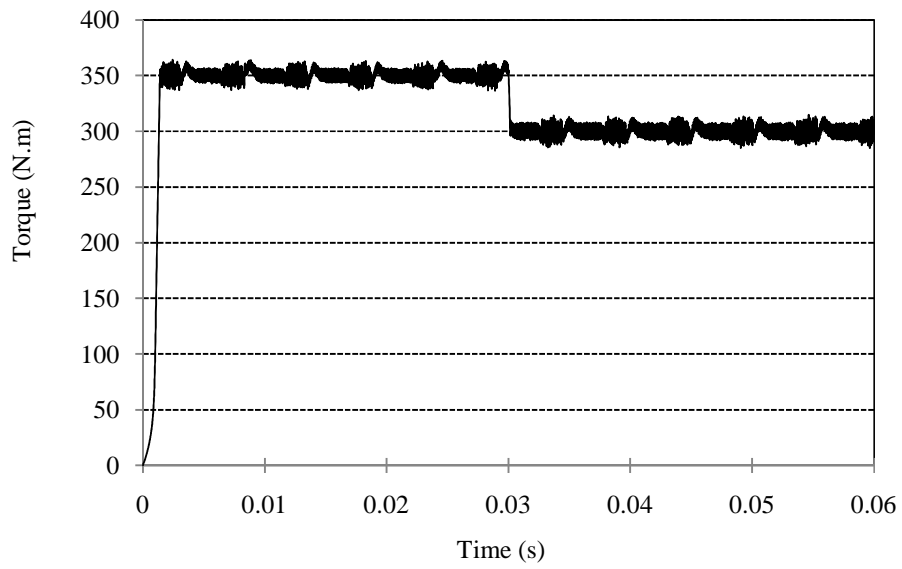

(b)

Fig. 4.9 Calculated waveforms at speed of 477.5 rpm with an initial torque command of 350 N.m changed to 300 N.m at 0.03 s.
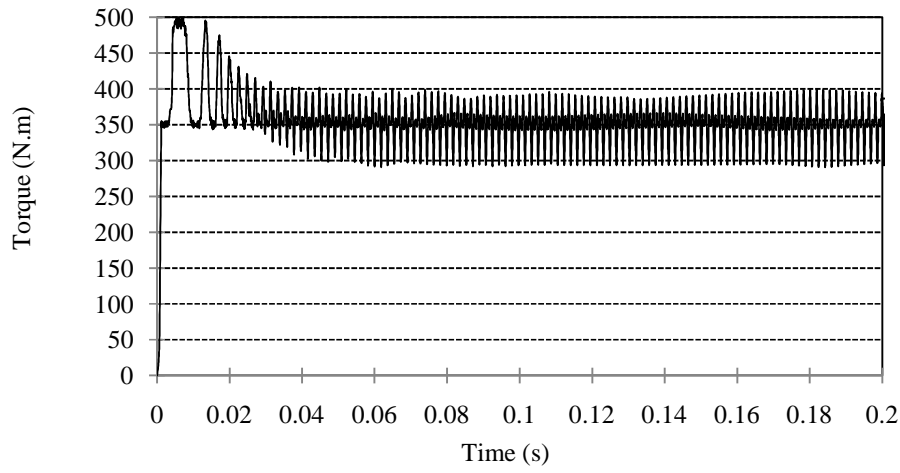**(a) 4-phase currents. (b) Output torque.**

4.3.3 Starting Performance with Load

It is also important to analyze the starting performance of a vehicle. During this starting period, the electric drive needs to produce a very high torque in a very short time. Fig. 4.10 shows the calculated results when the motor was started from standstill with load torque of 348 N.m. Fig. 4.10 (a) shows that the motor reaches the steady-state speed 1,380 rpm at 0.0541 s. It can be seen from Fig. 4.10 (b) that the average output torque is 349 N.m, which corresponds to the load torque of 348 N.m. However, during the starting, the torque ripple is higher compared with those in the steady-state and dynamic conditions. The reason is that training data for the BPNN controller are calculated from the static characteristic for unloaded condition.

Fig. 4.10 (c) shows that there is an overshoot in the phase current during starting. At this condition, the phase current is calculated to be 550 A, which is higher than the rated current 450 A. This is due to the fact that the motor requires larger power to accelerate during starting, the current drawn and the torque developed during starting are large which will reduce to values corresponding to the steady-state ones. The high starting output torque and current demonstrate that the motor should have short duration overload ability.
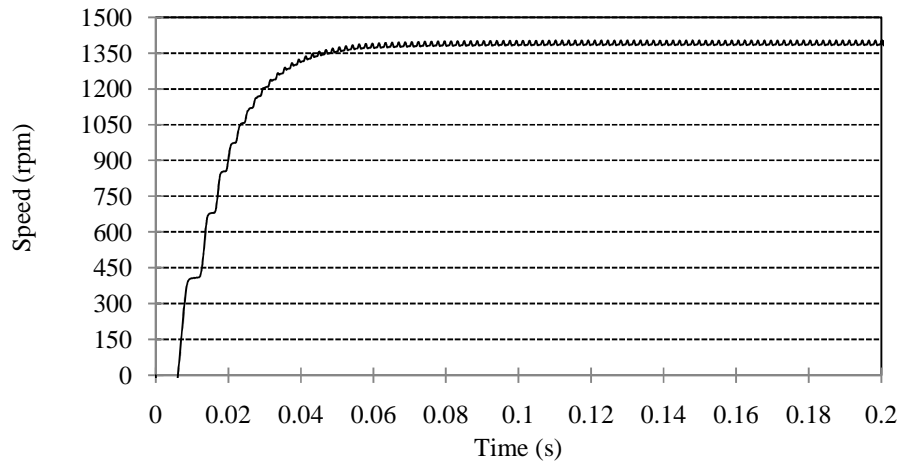
(a)

(b)
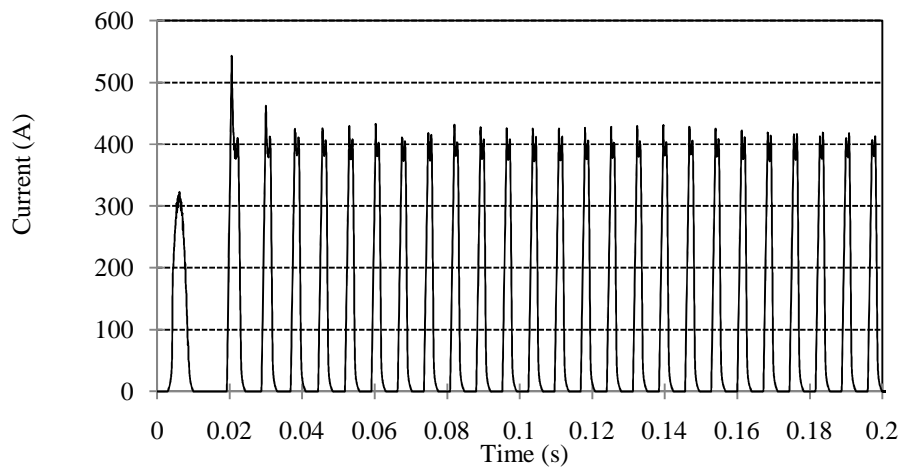
(c)

Fig. 4.10 Calculated waveforms for starting performance with a load torque of 348 N.m.
(a) Motor speed. (b) Output torque. (c) 4-phase currents.

5   EFFICIENCY OPTIMIZED TORQUE CONTROL OF SRM

5.1 Introduction

Although the torque ripple is the obvious drawback of the SRM which has been studied extensively, during high-speed operation, the large inertia of the vehicle can effectively smooth out the torque ripple of the SRM and the motor efficiency becomes the most important performance criterion of the vehicle drivetrain [58].

In this chapter, considering the extensive non-linearities in the losses of the power converter and torque characteristics of SRM, variation in the DC bus voltage, the extensive requirement for high efficiency at high speed, good dynamic performance and cost sensitivity of the HEVs traction application, a feed-forward back propagation neural network (BPNN) based direct inverse control is proposed to track the torque command while optimizing the motor efficiency at high speed for its simple structure, easy to implement and fast dynamics. A set of switching angles corresponding to specified operating points with maximum efficiency have been used to train the neural network. The problem of multi-valuedness related with the direct inverse control has been addressed by splitting the training data into several contiguous sets and designing a bank of two-hidden-layer neural network controllers for the high speeds. During real-time operation, the appropriate switching angles to optimize the motor efficiency are obtained by using the trained neural network controller. Computed results are presented to demonstrate the effectiveness of the proposed control scheme.

5.2 Design of Neural Network Based Controller

5.2.1   Diagram of the Controller

The diagram of the proposed BPNN-based torque controller is shown in Fig. 5.1. Neural network controller is used to track the torque and speed commands under certain DC voltage while optimizing the motor efficiency. By taking reliability, speed and cost into consideration, BP neural network is applied to calculate the appropriate turn-on and turn-off angles for the specified operation point. The commutation logic then selects the appropriate phases that will be conducted based on the instantaneous rotor position and

the switching angles. An asymmetric H-bridge converter is used to regulate the phase current for its simplicity and high stability.

5.2.2 Neural Network Controller

5.2.2.1 Training Data Acquisition

To build a neural network controller, the first step is to train the network. An offline dynamic simulation of SRM provides the training data for the neural network. The simulation is fulfilled in the following steps as shown in Fig. 5.2:
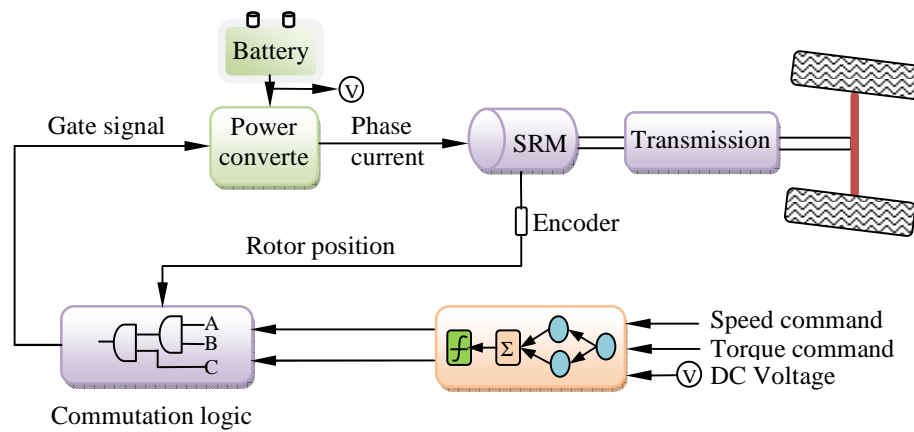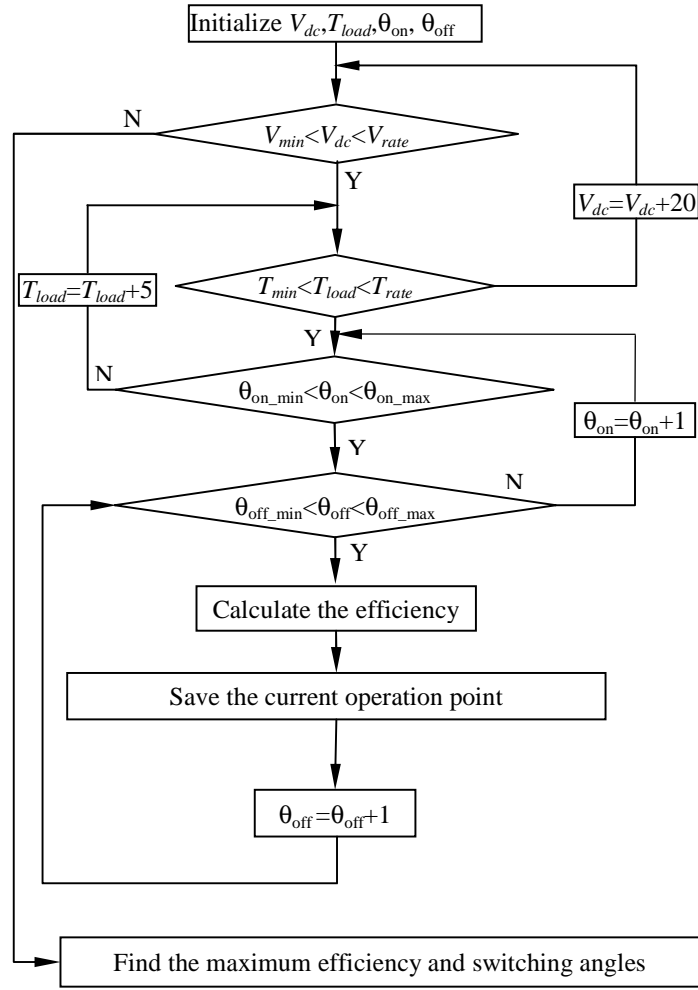

Fig. 5.1 Diagram of the proposed torque controller.

Fig. 5.2 Flow chart of training data acquisition.

(1) For a certain DC voltage and torque command, adjust all possible combinations of turn-on and turn-off angles to excite the SRM, calculate the motor efficiencies when the SRM is running at steady state by using (5.1)

$$\left.\begin{array}{l} \eta = \dfrac{P_{out}}{P_{in}} \times 100\% \\[2mm] = \dfrac{\omega T_{out}}{P_{in}} \times 100\% \end{array}\right\} \tag{5.1}$$

where T_{out} is the output torque, ω is the motor steady speed and P_{in} is the output power of the battery. All parameters used in (5.1) are RMS values.

(2) For a certain operation point (voltage, torque and motor speed), find the maximum efficiency and corresponding turn-on and turn-off angles.

(3) Find all possible pairs of turn-on and turn-off angles corresponding to all possible operation points with maximum efficiencies.

5.2.2.2   Neural Network Training

SRM will produce different torques when the rotor is running at different speeds and DC bus voltage under certain turn-on and turn-off angles. Obviously, in an inverse model of SRM, there are many different input data pairs (torque, speed and voltage) that will be mapped to one turn-on or turn-off angle which is called a multi-valued inverse mapping.

Generally, for this kind of model, during training, the feed-forward network tends to average the weights corresponding to various inputs, thereby cannot produce a high accuracy mapping [13]. After training, for a certain input data set (torque, speed and voltage), accurate turn-on and turn-off angles cannot be calculated from the inverse mapping. To make the inverse model learning the mapping properly, the training data have to be split into several data sets, and each data set is used to approximate one branch of the inverse model by using one neural network. Considering the complexity of a set of neural networks and the accuracy needed for torque tracking, the training data for the whole speed range up the base speed are divided into two data sets and used to train four neural networks, two neural networks are used to calculate the turn-on angle and the other two are used to calculate the turn-off angle.

As single-hidden-layer networks are not sufficient for stabilization, especially in discontinuous mapping, two-hidden-layer networks are enough assuming that bias units are used. In this work, for each neural network, a four-layer neural network comprising of an input layer, an output layer and two hidden layers is used. Levenberg-Marquard algorithm has been chosen to train the feed-forward neural networks due to its fast training speed. The training data have been divided into validation set and test set to get good generalization.
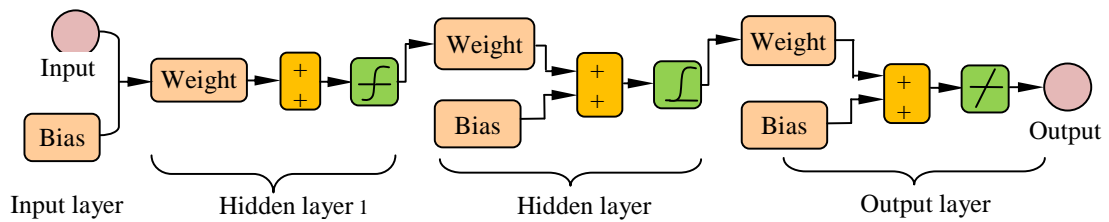
Fig. 5.3 Structure of one of the neural networks.

One of the neural networks is shown in Fig. 5.3. The input layer has bias and three input units which are DC voltage, speed and torque command, and the output layer has one output unit which is either turn-on angle or turn-off angle. The activation functions for the hidden layer 1 are hyperbolic tangent sigmoid function and log-sigmoid functions are for hidden layer 2, the output layer activation function is linear transfer function, and the learning function is gradient descent with momentum weight and bias learning function.

5.3 Simulation Results and Analysis

The proposed SRM torque controller has been simulated by using the motor described in Appendix A1 in Matlab/Simulink as shown in Fig. 5.4. Corresponding to different conditions in the propulsion, the performances of the SRM drive are calculated and analyzed when it is running at different conditions such as steady-state and dynamic state.
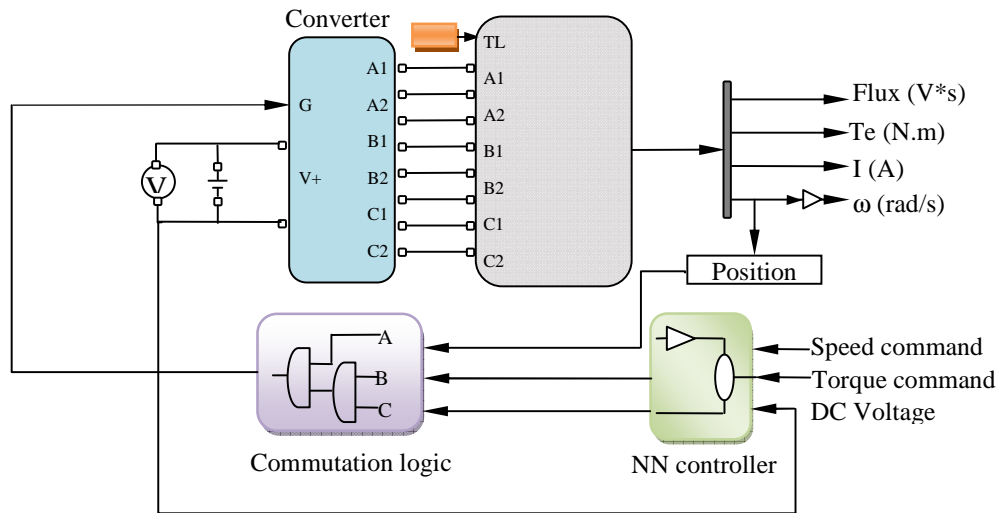
Fig. 5.4 Simulation model of NN torque controller.

5.3.1 Drive Performance at Different DC Voltages

Drive performance at different DC voltage levels under steady-state condition has been investigated. Figs. 5.5 and 5.6 present the speed and efficiency maps under load torque of 150 N.m with DC voltage of 240 V and 220 V, respectively. Both Fig. 5.5 (a) and Fig. 5.6 (a) show that the turn-on angle should be advanced to provide additional time for currents to build up in order to produce enough torque when the motor is running at high speeds. This advance creates more negative torque, but the additional negative torque is more than off-set by the increase in position torque. As to the turn-off angle, it has to be chosen to ensure that the current in the off-going phase has enough time to vanish. If not, the off-going phase will produce negative torque and the efficiency of the motor will be very low as shown in Fig. 5.5 (b) and Fig. 5.6 (b). When excited under the same turn-on and turn-off angles with same load torque, motor runs at lower speed under lower voltage with similar efficiency which shows that the drive efficiency is not sensitive to the changes of the supply voltage.
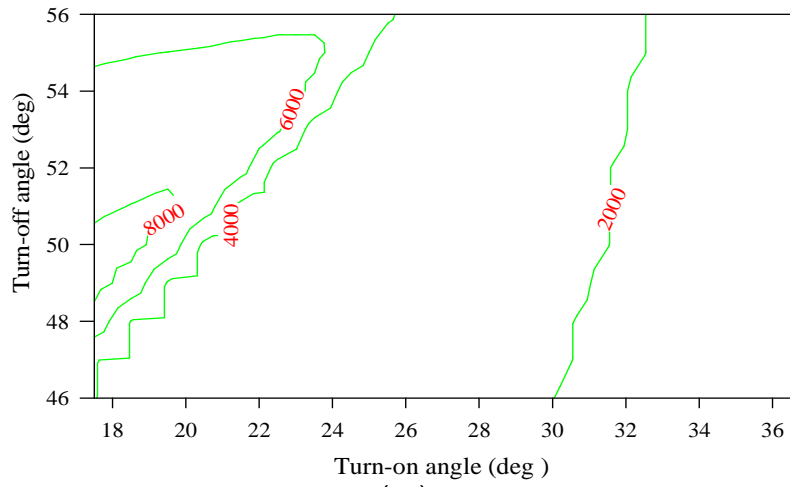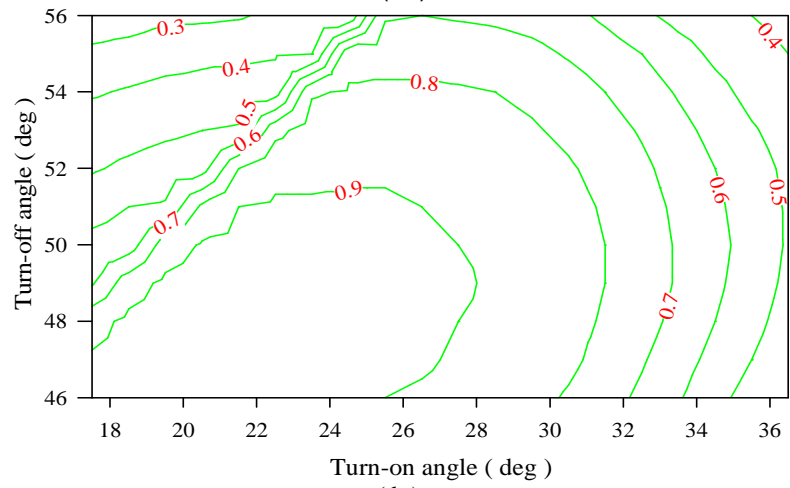
Fig. 5.5 Efficiency and speed maps for V=240 V, T=150 N.m.
(a) Speed map. (b) Efficiency map.
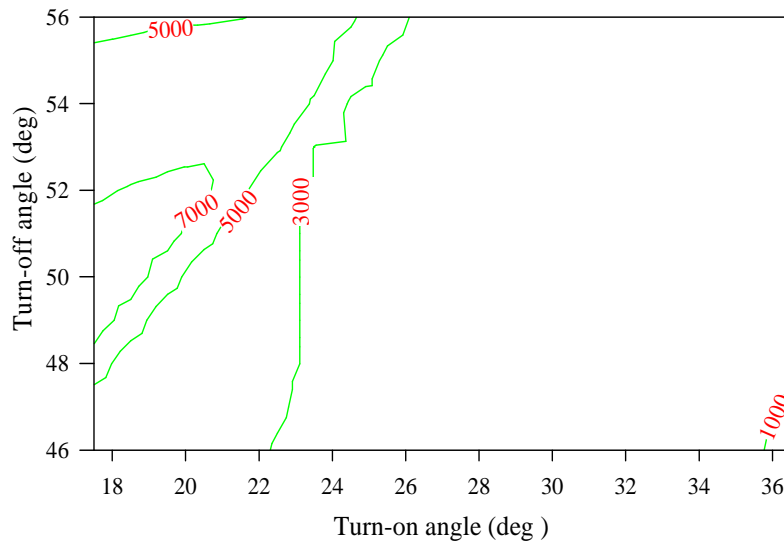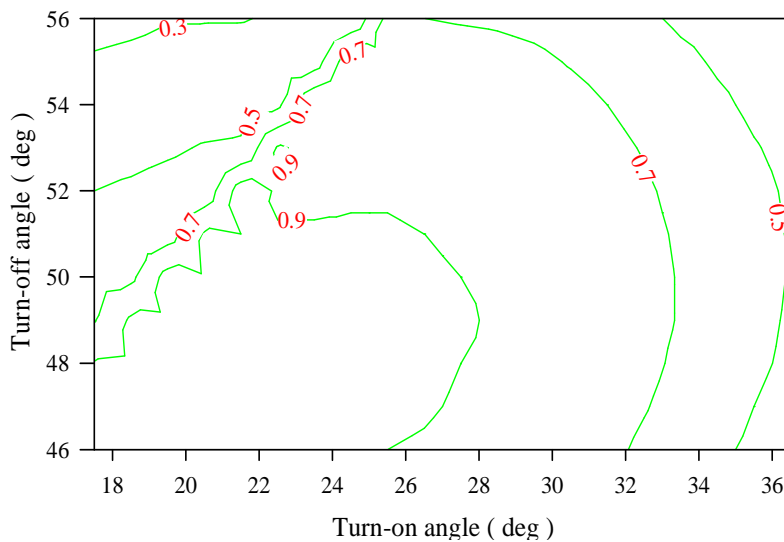
Fig. 5.6 Efficiency and speed maps for V=220 V, T=150 N.m.
(a) Speed map. (b) Efficiency map.

5.3.2 Steady-State Performance

During most of the time, vehicle runs at steady-state under constant load. The vehicle control unit expects a precise and stationary average torque of the electric drive which can track precisely the reference torque with high efficiency.

To analyze the controller performance under steady-state, the torque command was set to 160 N.m, the motor speed was 3,630 rpm with load torque of 156.2 N.m. Motor efficiency, torque output under this operating condition are shown in Fig. 5.7. Fig. 5.7(b) shows that the average torque output reaches 160.6 N.m with efficiency around 0.91 when the turn-on angle is 19.49^o and turn-off angle is 47.16^o.
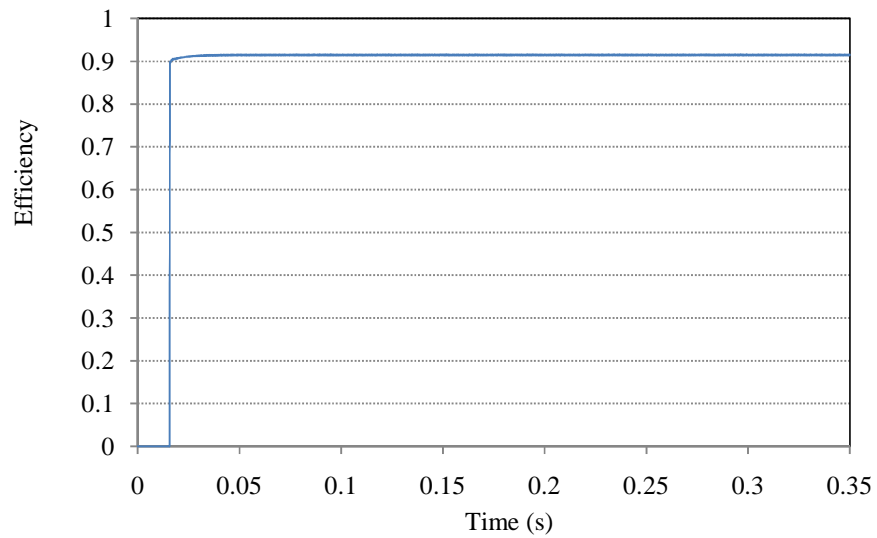
(a)
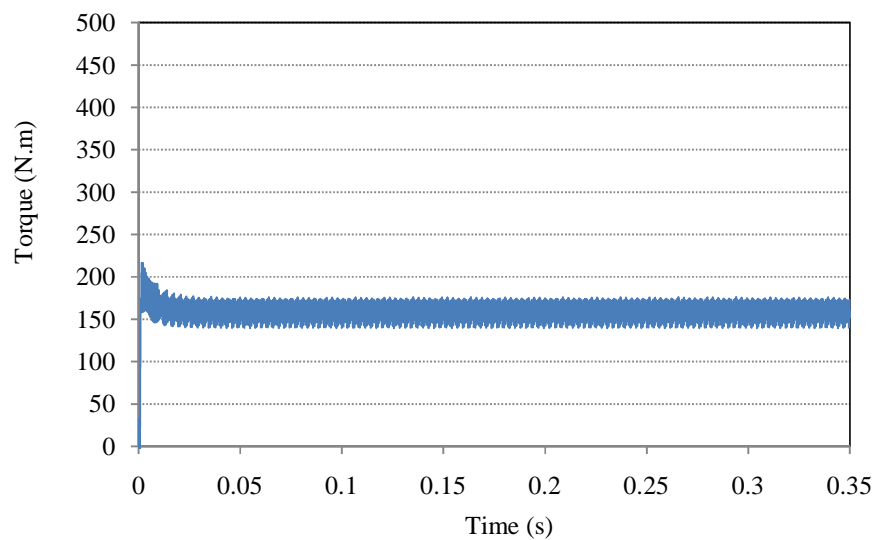
(b)

Fig. 5.7 Calculated waveforms at speed (3,630 rpm) with a torque command of 160 N.m. (a) Motor efficiency. (b) Torque output.

5.3.3 Dynamic Performance

While the vehicle is running at constant speed like under cruise control, the load torque can vary abruptly due to the change of the road condition. When the vehicle is running at this kind of state, the control unit also expects a precise average torque and fast system response from the electric drive.

In the dynamic performance simulation, the motor speed is set to be 3,630 rpm while the output torque changes from 140 N.m to 185 N.m at 0.2 s. One phase current is shown in Fig. 5.8(a) which cannot reach rated current; the higher torque the motor produces, the higher phase current the motor needed which can be reached by advancing the turn-on angle and postponing the turn-off angle as shown in Fig. 5.8(b). It is shown in Fig. 5.8(c) that T_{out} increases to 185.0 N.m at 0.2007 s, which means that the dynamic performance of the controller is very good. The torque ripple of the drive is high around 30% as presented in Fig. 5.8(c) due to the switching control. But under high speed, this kind of ripple is acceptable considering the high vehicle inertia.
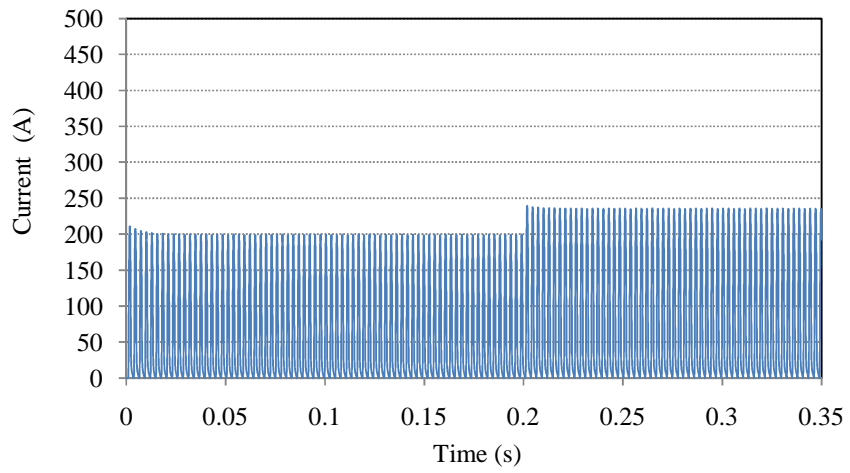
(a)
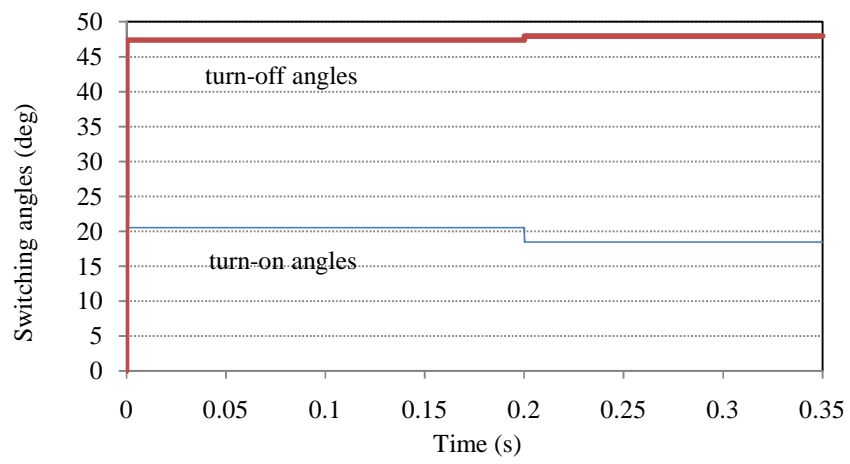
(b)
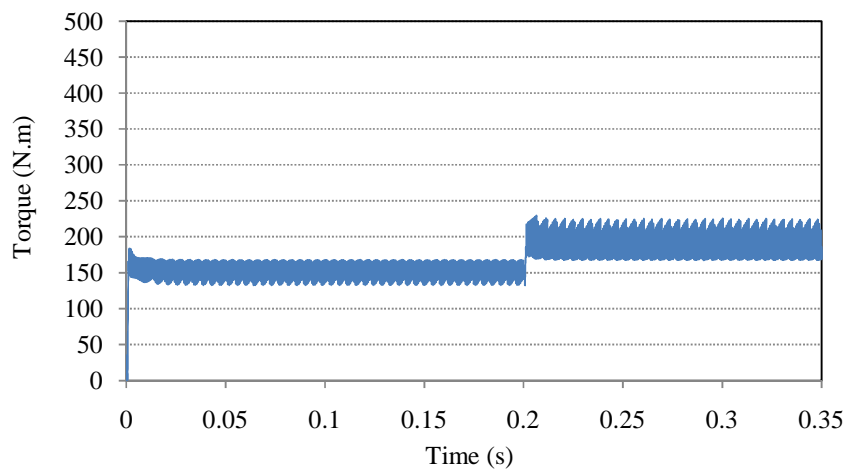
(c)

Fig. 5.8 Calculated waveforms for motor speed of 3,630 rpm with torque command changed from 140 N.m to 185 N.m at 0. 2 s.
(a) One phase current. (b) Switching angles. (c) Torque output.

6 TORQUE CONTROL OF SRM FOR THE WHOLE SPEED RANGE

6.1 Introduction

A comprehensive torque controller is in extremely high demand for SRM which can offer low torque ripple at low speed, high efficiency at high speed, good dynamic performance and low cost. The vehicle control unit always expects a precise and stationary average torque of the electric drive which tracks precisely the reference torque to perform dynamic assistance regulating tasks, such as anti-slip traction and braking control. Average torque is the torque averaged over one stroke ($2*\pi/m*N_r$, m is the number of motor phases, N_r is the number of the motor rotors) which requires a lower control-loop bandwidth than instantaneous torque control. Average torque can be controlled by varying many control variables such as phase currents, switching angles or both, but the configuration depends on the performance requirements, the acceptable level of complexity, and the cost. Since there are many possible combinations of control variables which produce the same torque, a secondary control objective is needed to select and define the variation of control variables for optimum performance such as efficiency and torque ripple.

For the HEV traction application, at low speeds range, the torque ripple is the obvious drawback of the SRM which has been studied extensively. During high-speed operation, the large inertia of the vehicle can effectively smooth out the torque ripple of the SRM and the motor efficiency becomes the most important performance criterion of the vehicle drive-train [58]. The criteria for the whole speed range torque control of SRM should be low torque ripple at low speeds and high power efficiency at high speeds.

At lower speeds, the torque is limited only by the current, which is regulated either by voltage-PWM, or instantaneous current regulation. As the speed increases, the back-EMF increases to a level at which there is insufficient voltage available to regulate the current; only the timing of the current pulses or switching angles can then be used to control the torque. However, a change of control strategy or stepwise change of the switching angles may result in a sudden change of the average machine torque which will

generate oscillations in the drive-train where smooth transition between the SRM operations is highly required.

In this research, a torque controller of SRM for the whole speed range to satisfy the requirement of HEV traction application has been investigated; methods to reduce the torque/speed oscillation have been considered. Extensive simulations have been done to evaluate the performance of the proposed controller.

6.2 Design of the BPNN-based Whole Speed Range Torque Controller

6.2.1 Diagram of the Controller

The diagram of the proposed BPNN-based torque controller is shown in Fig. 6.1. An asymmetric H-bridge converter is used to excite the phases of SRM by following the gate signal for its simplicity and high stability. Two BPNN controllers are used to track the torque and speed commands under certain DC bus voltage: one described in Chapter 4 is applied to calculate the phase currents at low speeds to minimize the torque ripple, while the other one described in Chapter 5 is used to acquire the appropriate turn-on and turn-off angles for the specified operation point to ensure optimized motor efficiency at high speeds. To ensure seamless transition between the two operation modes, two blocks have been applied: speed dead-band filter and firing angle adjusting block.
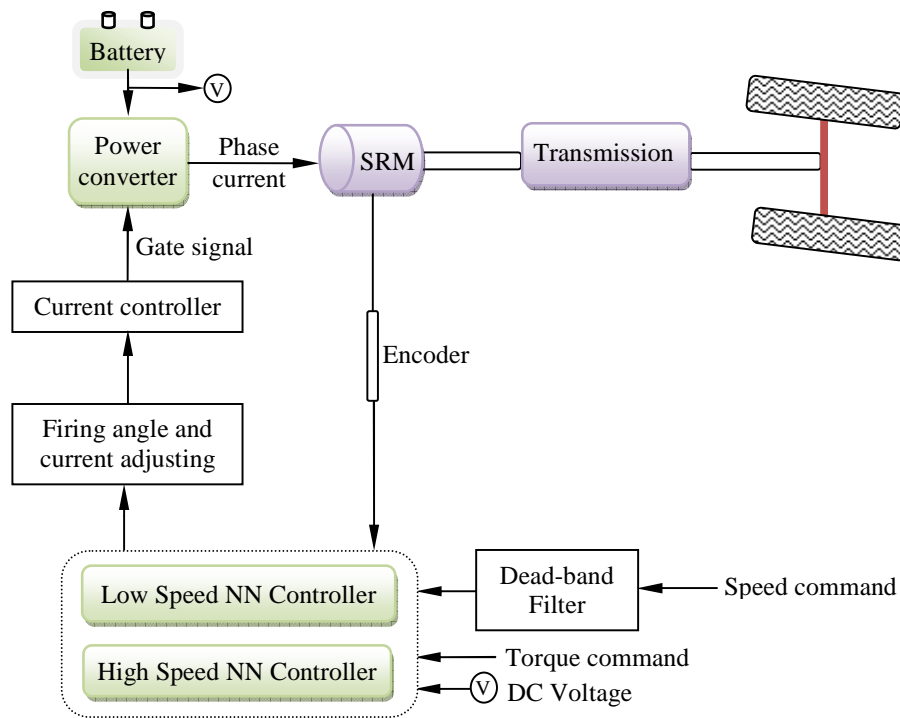
Fig. 6.1 Diagram of the proposed controller.

6.2.2   Dead-band Filter

A dead-band is an area of a signal range or band where no action occurs. The purpose is to prevent oscillation or repeated activation-deactivation cycles. Fig. 6.2 shows the principle of dead-band filter. When the commanded speed is transient around the base speed within a selected range, the control mode will not change. If it is changed from less-than-base-speed to over-base-speed, the control mode will change to high-speed control mode; afterwards, if it is not lower than the low-bound, the control will continue to be high-speed mode. Vice versa, if the commanded speed is changed from over-base-speed to less-than-base-speed, the control mode will change to low-speed control mode, afterwards, if it is not higher than the up-bound speed, the control will stay with low-speed mode.
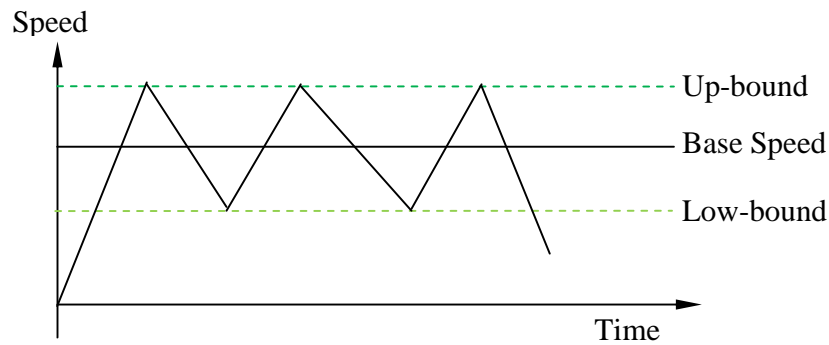
Fig. 6.2 Principle of dead-band filter.

6.2.3 Firing Angles and Phase Current Adjusting

As the speed increases, the back-EMF increases to a level at which there is insufficient voltage available to regulate the current, only the timing of the current pulses or firing angle can then be used to control the torque. However, the change of firing angle will break the rhythm of switching on the phases; big oscillations of shaft torque output can be observed when the turn-on angle is changed in increments of more than one mechanical degree. To avoid this kind of oscillations, a continuous change of the firing angles and phase currents has to be applied, which will slow down the response of the controller when big change of turn-on angle is required. However, for HEV traction application which always has an acceleration time, this can be endurable.

6.3 Performance Evaluation through Simulation

The proposed SRM torque controller has been simulated by using the motor described in Appendix A1 in Matlab/Simulink. As the controller performance such as starting, steady-state at low speeds and high speeds, dynamic response in the low speed range and high speed range have been simulated and analyzed in previous chapters, the following simulation will be done to validate the performance when the motor speed is changing from low speed to high speed with and without firing angle adjusting, and the performance when the bus-voltage is changed.

### 6.3.1 Performance with Changing of Control Mode

At lower speeds, the torque is limited by the switching angles and phase currents regulated by the hysteresis current controller. However, at high speeds, the SRM turns into single-pulse mode because the motor's back EMF is larger than the dc-link voltage, and the torque is controlled by properly adjusting the firing angles of a single-current pulse.

In the dynamic performance simulations shown in Fig. 6.3, the command torque, T_{com}, was changed from 250 N.m to 85 N.m at 0.2 s and, the command speed, ω_{com}, was changed from 1,310 rpm to 7,600 rpm at the same time. After the controller received the command and adjusted the control parameter for the final command to export more power, the phase current has been adjusted to the rated current as shown in Fig. 6.3(a), and switching angles have been adjusted to export more power to meet the requirements. However, due to the inertia of the motor, the motor can only speed up gradually as shown in Fig. 6.3(b) which results in a big spike of about 550 N.m in the shaft torque shown in Fig. 6.3(c). Fig. 6.3(d) shows that the firing angle has been advanced to 17.5° which is beyond the point where the dwell angle becomes equal to about half the rotor pole-pitch, continuous conduction begins at this point and the phase current never falls to zero as shown in Fig. 6.3(a). By running at continuous conduction mode, the phase currents can go up to rated current and the motor will increase the power density. The penalty is an increase in copper loss, which is acceptable if there is a greater gain in converted power and the machine can withstand the temperature rise.

By gradually adjusting the turn-on angle and the phase current as shown in Figs. 6.4(a) and (b), the torque output decreases gradually from 230 N.m to around 100 N.m with the steadily increasing speed as shown in Figs. 6.4(c) and (d). The maximum torque reduces from 550 N.m to 230 N.m. However, due to the adjustment, the response time of the motor drive is getting longer which is acceptable for HEV traction application considering the response time of the driver and the vehicle.

(a)

(b)
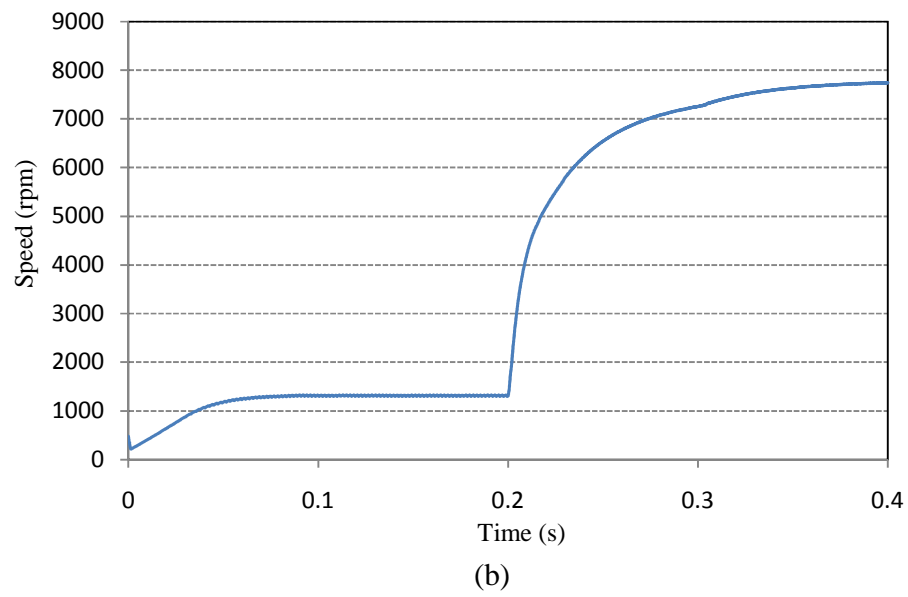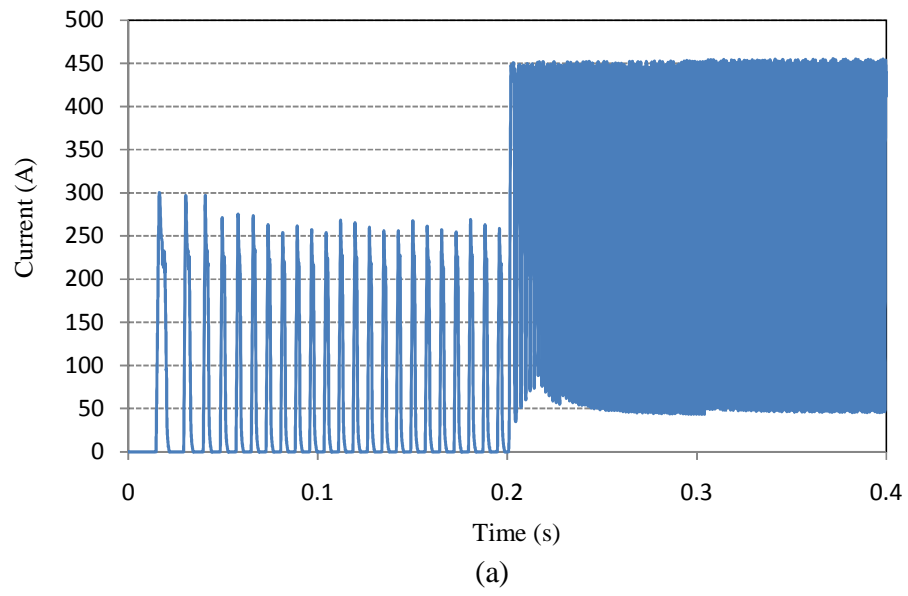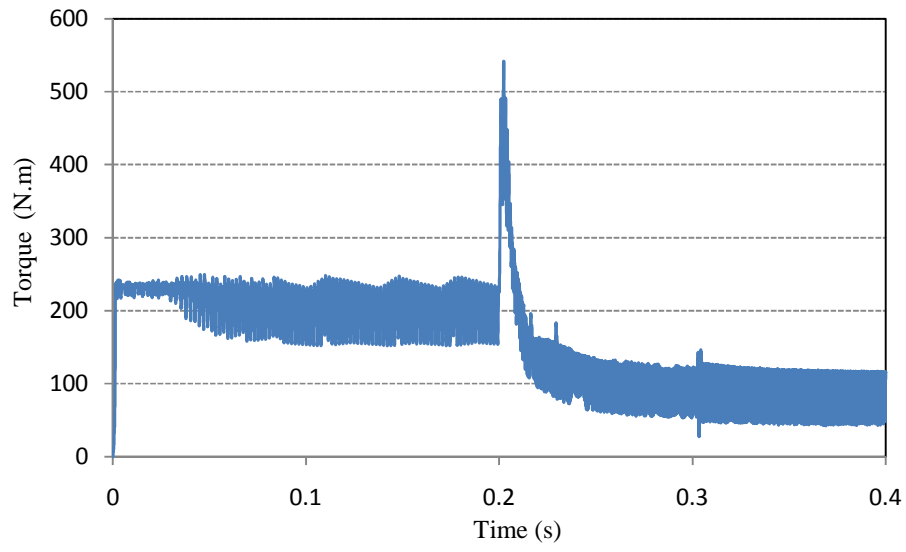
(c)
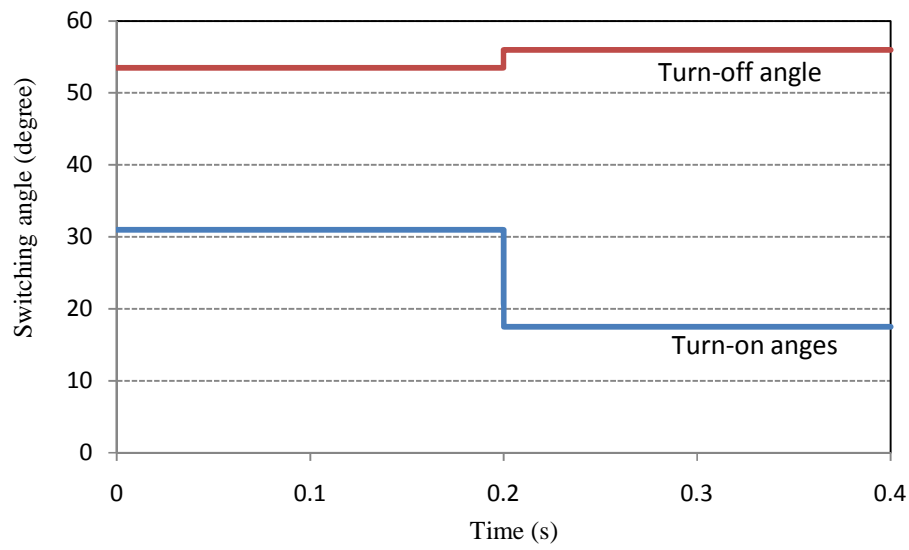
(d)

Fig. 6.3 Calculated waveforms when torque command changed from 230 N.m to 85 N.m and speed command changed from 1,310rpm to 7,600rpm at 0.2 s without the firing angle adjusting. (a) One phase current. (b) Motor speed. (c) Torque output (d) Switching angles
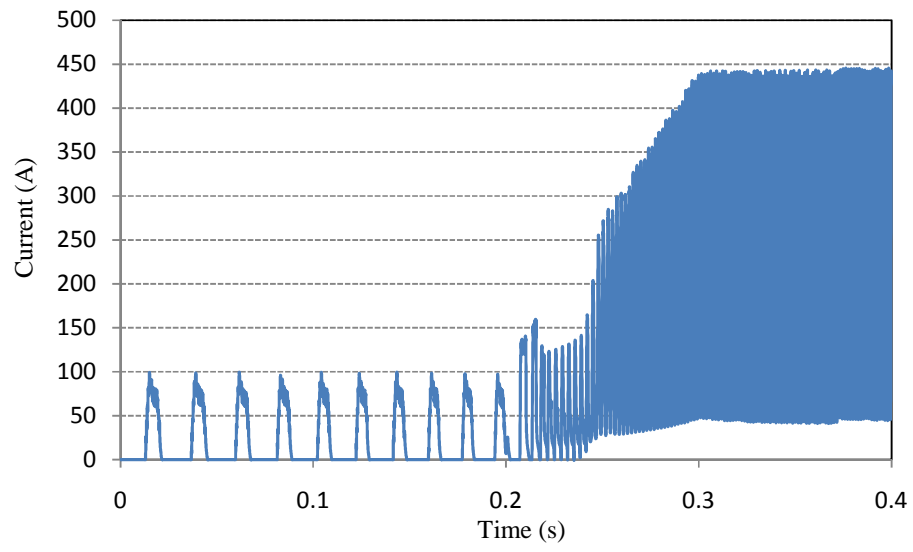
(a)
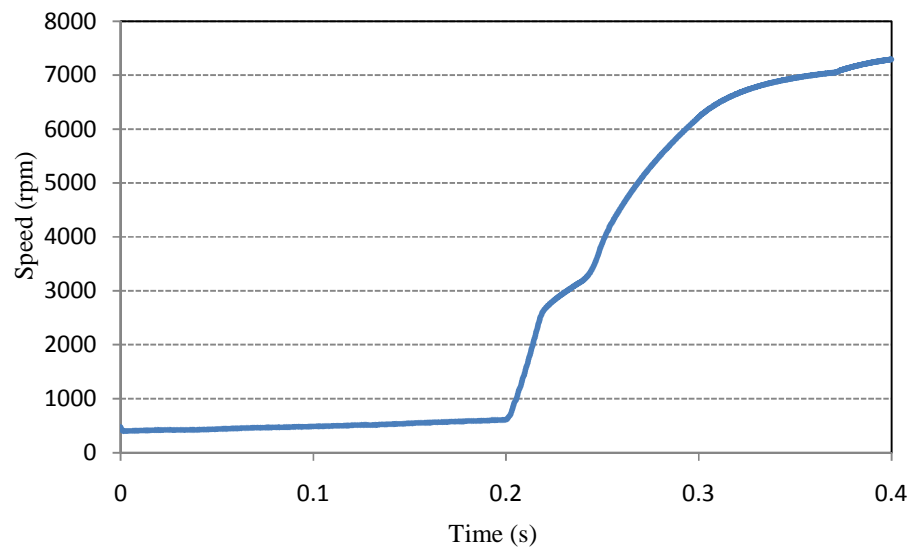
(b)
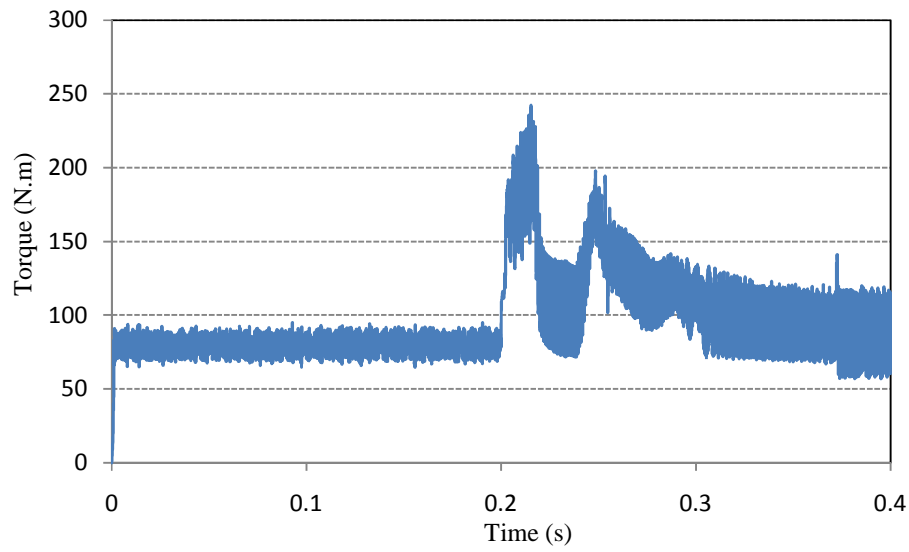
(c)
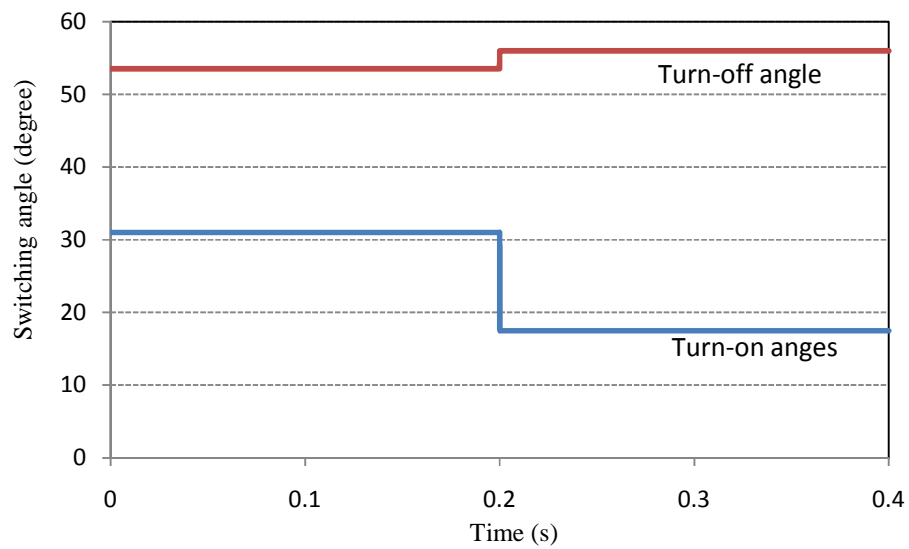
(d)

Fig. 6.4 Calculated waveforms when torque command changed from 230 N.m to 85 N.m and speed command changed from 1,310rpm to 7,600rpm at 0.2 s with the firing angle adjusting. (a) One phase current. (b) Motor speed. (c) Torque output (d) Switching angles

6.3.2 Performance under Changing of DC Bus Voltage

While the vehicle is running at constant speed like under cruise control, the DC bus voltage can vary abruptly due to the change of SOC of the battery. However, the

control unit always expects a precise average torque and also fast response from the electric drive, the control parameter of the motor drive have to be adjusted to meet the command.

In the simulation, in order to validate the performance related with the change of the DC bus voltage, the speed and torque were kept constant respectively of 5,064 rpm and 165 N.m while the DC bus voltage was changed from 240 V to 220 V. The simulated waveforms are shown in Fig. 6.5. When the DC bus voltage changed, based on the calculation of the BPNN controller, the switching angles, which are shown in Fig. 6.5(d), were adjusted corresponding to the change. Due to the big change of the firing angles, firing angle adjusting was applied.

It is clear as shown in the simulation that when the DC bus voltage is decreasing, the firing angles have to be advanced to give the phase current enough time to increase to meet the power demand. Also, the turn-off angles are not sensitive to the change of the DC bus voltage which is reasonable as the turn-off angles usually affect the decaying time of the phase current.
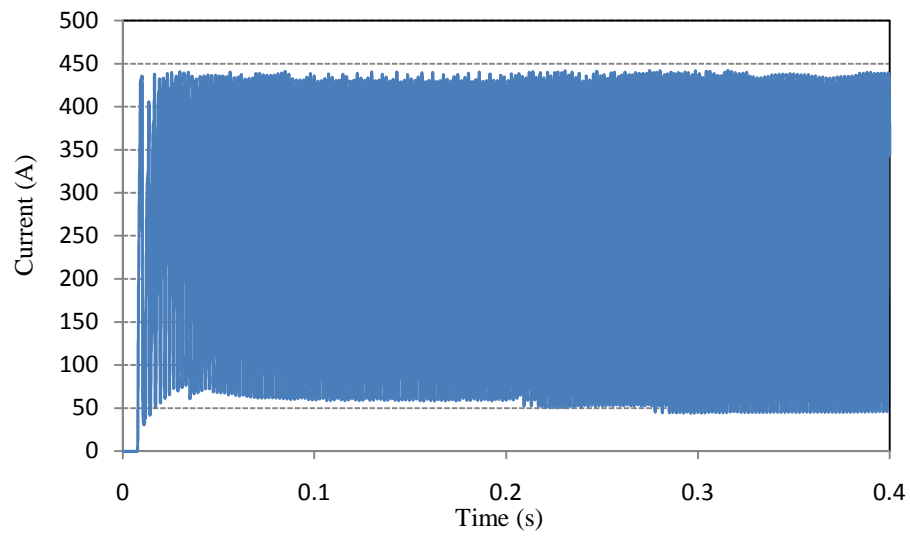
(a)
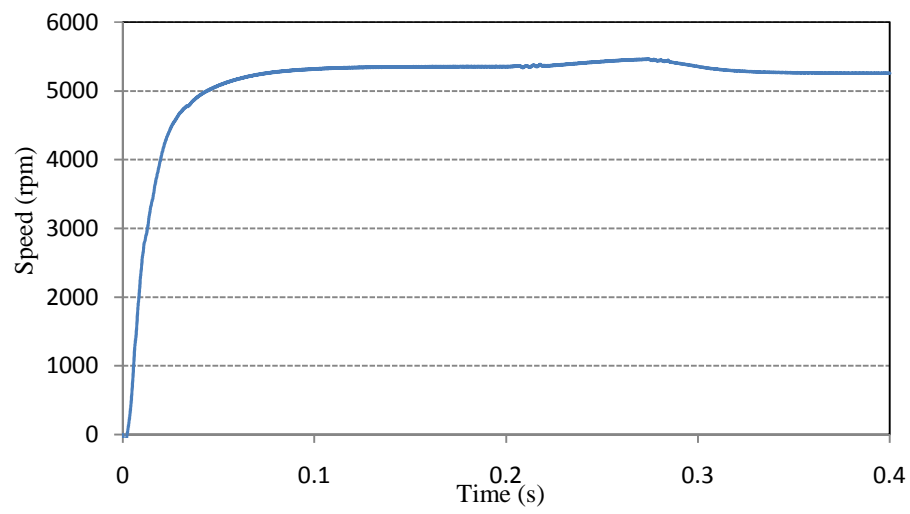
(b)
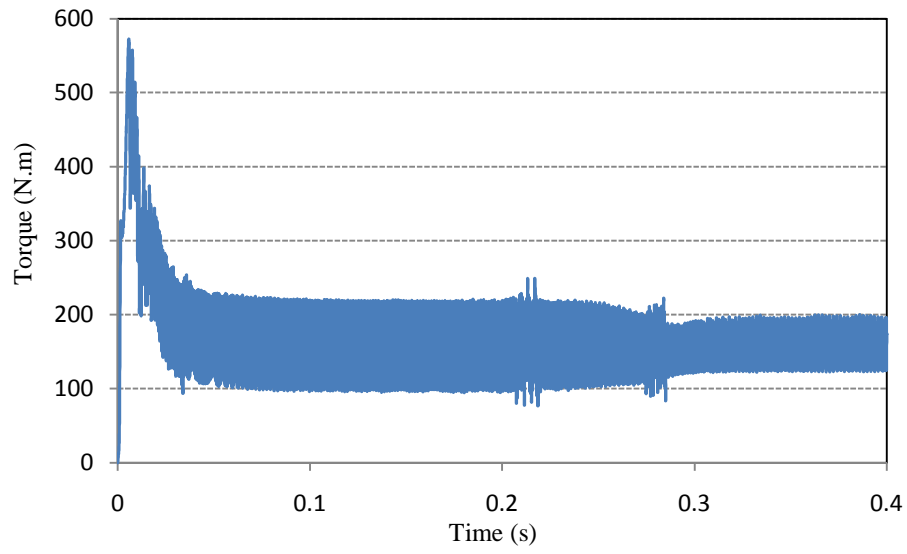
(c)
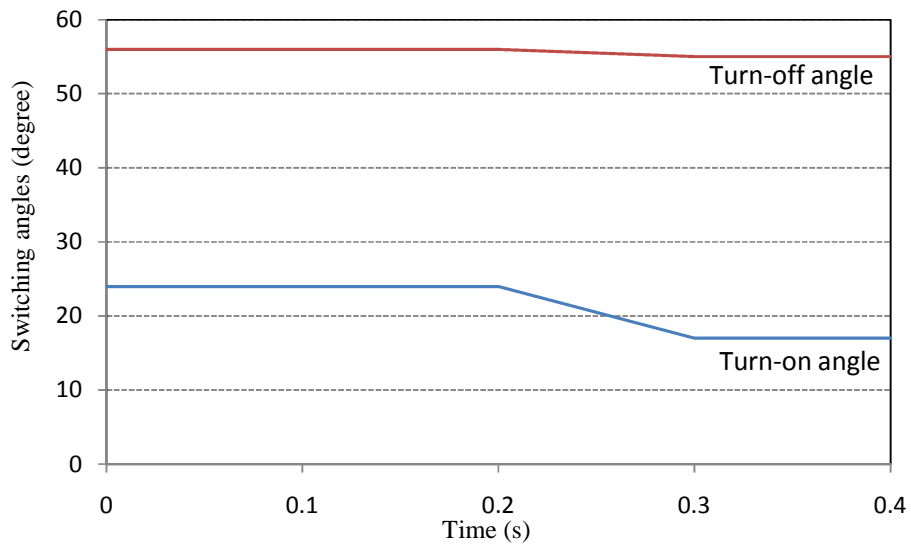
(d)

Fig. 6.5 Calculated waveforms when DC bus voltage changed from 240 V to 220 V.
(a) One phase current. (b) Motor speed. (c) Torque output (d) Switching angles

7 CONCLUSIONS AND FUTURE WORK

7.1 Conclusions

Motivated by a desire to find an alternative vehicle which is independent on the petroleum, environment friendly and affordable, HEVs have been successfully launched commercially by major automakers. The performance of HEVs heavily relies on the development of drive train, specifically, the traction motor. Hence, this research is focused on the torque control of SRM, one of the suitable traction motors for HEV application, to reduce the torque ripple at low speeds and improve the power efficiency at high speeds.

Based on the analysis of the nonlinearity torque-current-position characteristics of the SRM and the high generalization ability of the BPNN based control algorithm, a bank of BPNNs based torque controller has been proposed. The methodology to acquire the training data and to train the neural network has been presented. A set of neural networks is applied to get an accurate inverse model of SRM. To generate smooth torque output responding to the torque/speed command from energy management system of the HEVs, speed dead-band filter and gradually varied phase currents and firing angle have been applied to the controller. It has been demonstrated that the proposed controller has the following advantages:

(1) Offer the ability of torque control in the motor's whole speed range.

(2) Exhibit good steady-state and dynamic performances responding to the changes of the torque command, speed command and DC-bus voltage.

(3) Produce maximum torque quickly during starting while requiring short duration overload ability.

(4) Generate smooth torque output while tracking the command changes with high accuracy at low speeds.

(5) Demonstrate high ability to follow the high efficiency track of the motor at high speeds.

(6) Reduce torque oscillation when the control mode is changed.

7.2 Future Work

This research clearly demonstrates the potential of neural network based torque control of SRM for HEV traction application. However, there are certain areas which would require further research.

The neural network used in this research is back-propagation neural network, whose weights are fixed during real-time operation. Other kind of intelligent control method such as neural fuzzy system can be investigated to improve the flexibility and adaptability of the controller.

Generally, open-loop torque control proposed in this research is acceptable for HEV traction application. However, close-loop torque control can also be investigated to improve the drive performance for high-end vehicle. Neural networks which can update the weights on-line can be used in this kind of neural network controller.

Another problem area for SRM is the acoustic noise. Appropriate commutation control can help to reduce the noise level. A successful control algorithm, which can reduce the torque ripple and noise and improve the power efficiency, will improve the performance of the SRM drive train for the HEV traction application.

APPENDIX A   MOTOR PARAMETERS

The parameters of an 8/6 SRM from the library of MATLAB/SIMULINK is shown in the following table:

Nominal power	75 kW
No. of stator poles	8
No. of rotor poles	6
No. of phases	4
Stator resistance	0.01 Ω
Friction constant	0.01 N.m.s
Unaligned inductance	0.67×10^{-3} H
Aligned inductance	23.6×10^{-3} H
Saturated aligned inductance	0.15×10^{-3} H
Inertia constant	0.0082 kg-m^2
Maximum current	450 A
Maximum flux linkage	0.486 V.s

APPENDIX B   LIST OF PUBLICATIONS

[1]   D. Lu and N. C. Kar, "Neural network based torque control of switched reluctance motor for hybrid electric vehicle propulsion at low speeds," in *Proc. IEEE Electro/Information Technology Conference,* pp.417-422, 2009.

[2]   D. Lu and N. C. Kar. "Neural network based torque control of switched reluctance motor for hybrid electric vehicle propulsion at high speeds," in *Proc. IEEE Electrical Power and Energy Conference*, 2009.

REFERENCES

[1] J. M. Miller, *Propulsion Systems for Hybrid Vehicles*, London: The Institution of Electrical Engineers, 2004.

[2] Y. Gao and M. Ehsani, "An investigation of battery technologies for the Army's hybrid vehicle application," in *Proc. of the IEEE 56th Vehicular Technology Conference*, 2002.

[3] M. Ehsani, Y. Gao, S. E. Gay, and A. Emadi, Modern Electric, Hybrid Electric, and Fuel Cell Vehicles: Fundamentals, Theory, and Design, Boca Raton: CRC Press, 2005.

[4] M. Zeraoulia, M. E. H. Benbouzid, and D. Diallo, "Electric motor drive selection issues for HEV propulsion systems: A comparative study," *IEEE Trans. on Vehicular Technology*, vol. 55, pp. 1756-1764, Nov. 2006.

[5] Husain, *Electric and Hybrid Vehicles - Design Fundamentals*, Boca Raton: CRC Press, 2003.

[6] P. Mongeau, "Traction motor applications," in the Ground-Automotive Power & Energy Symposium, July, 2005.

[7] S. Henneberger, U. Pahner, K. Hameyer, and R. Belmans, "Computation of a highly saturated permanent magnet synchronous motor for a hybrid electric vehicle," *IEEE Trans. on Magnetics*, vol. 33, part 2, pp. 4086-4088, Sept. 1997.

[8] B. Stumberger, A. Hamler, M. Trlep, and M. Jesenik, "Analysis of interior permanent magnet synchronous motor designed for flux weakening operation," *IEEE Trans. on Magnetics*, vol. 37, part 1, pp. 3644-3647, Sept. 2001.

[9] M. E. H. Benbouzid and N. S. Nait Said, "An efficiency-optimization controller for induction motor drives," *IEEE Power Engineering Letters*, vol. 18, no. 5, pp. 43-45, May 1998.

[10] S. Z. Jiang, K. T. Chau and C. C. Chan, "Spectral analysis of a new six-phase pole-changing induction motor drive for electric vehicles," *IEEE Trans. Industrial Electronics*, vol. 50, no. 1, pp. 123-131, Feb. 2003.

[11] J. W. Kelly, E. G. Strangas and J. M. Miller, "Control of a continuously operated pole-changing induction machine," in *Proc. IEEE International Electric Machines and Drives Conference*, pp. 211-217, 2003.

[12] 2010 Tesla Roadster.

[Online]. Available: http://www.teslamotors.com/performance/perf_specs.php

[13] M. Krishnamurthy, C. S. Edrington, A. Emadi, P. Asadi, M. Ehsani, and B. Fahimi, "Making the case for applications of switched reluctance motor technology in automotive products," *IEEE Trans. on Power Electronics*, vol. 21, pp. 659-675, May 2006.

[14] C. S. Edrington, M. Krishnamurthy, and B. Fahimi, "Bipolar switched reluctance machines: A novel solution for automotive applications," *IEEE Trans. on Vehicular Technology*, vol. 54, pp. 795-808, May 2005.

[15] S. Wang, Q. Zhan, Z. Ma, and L. Zhou, "Implementation of a 50-kW four-phase switched reluctance motor drive system for hybrid electric vehicle," *IEEE Trans. on Magnetics*, vol. 41, part 2, pp. 501-504, Jan. 2005.

[16] K. M. Rahman, B. Fahimi, G. Suresh, A. V. Rajarathnam, and M. Ehsani, "Advantages of switched reluctance motor applications to EV and HEV: Design and control issues," *IEEE Trans. on Industry Applications*, vol. 36, pp. 111-121, Jan. -Feb. 2000.

[17] D. -H. Lee, Z. -G. Lee, J. Liang, and J. -W. Ahn, "Single-phase SRM drive with torque ripple reduction and power factor correction," *IEEE Trans. on Industry Applications*, vol. 43, pp. 1578-1587, Nov. -Dec. 2007.

[18] M. Khan, "Study of Challenges in Technology Development and Market Penetration of Hybrid Electric Vehicles in Canada," MASc. Thesis, Dept. ECE, University of Windsor, Canada, 2009.

[19] Ozawa, T. Kosaka, and N. Matsui, "Less rare-earth magnet-high power density hybrid excitation motor designed for hybrid electric vehicle drives," in *Proc. European Conference on Power Electronics and Applications*, pp. 1-10, September, 2009.

[20] J. S. Hsu, C. W. Ayers, and C. L. Coomer, "Report on Toyota/Prius Motor Design and Manufacturing Assessment," Oak Ridge National Laboratory, 2004.

[21] Labak and N. C. Kar, "A novel five-phase pancake shaped switched reluctance motor for hybrid electric vehicles," in *Proc. IEEE Conference on Vehicle Power and Propulsion*, pp. 94-499, September, 2009.

[22] X. D. Xue, K. W. E. Cheng, and S. L. Ho, "A control scheme of torque ripple minimization for SRM drives based on flux linkage controller and torque sharing function," in *Proc. 2nd International Conference on Power Electronics Systems and Applications*, pp. 79-84, 2006.

[23] J. M. Stephenson, A. Hughes, and R. Mann, "Online torque-ripple minimisation in a switched reluctance motor over a wide speed range," *IEE Proc. on Electric Power Applications*, vol. 149, no. 4, pp. 261-267, 2002.

[24] C. Shang, D. Reay, and B. Williams, "Adapting CMAC neural networks with constrained LMS algorithm for efficient torque ripple reduction in switched reluctance motors," *IEEE Trans. on Control Systems Technology*, vol. 7, No. 4, pp. 401-413, July 1999.

[25] Z. Lin, D. S. Reay, B. W. Williams, and X. He, "Torque ripple reduction in switched reluctance motor drives using B-spline neural networks," *IEEE Trans. on Industry Applications*, vol. 42, no. 6, pp. 1445-1453, Nov.-Dec. 2006.

[26] J. G. O'Donovan, P. J. Roche, R. C. Kavanagh, M. G. Egan, and J. M. D. Murphy, "Neural network based torque ripple minimisation in a switched reluctance motor," in *Proc. 20th International Conference on Industrial Electronics, Control and Instrumentation*, vol.2, pp. 1226-123, 1994.

[27] K. M. Rahman A. V. Rajarathnam and M. Ehsani, "Optimized instantaneous torque control of switched reluctance motor by neural network," *IEEE Industry Application Society Annual Meeting*, pp. 556-563, 1997.

[28] Y. Cai and C. Gao, "Torque ripple minimization in switched reluctance motor based on BP neural network," in *Proc. 2nd IEEE Conference on Industrial Electrics and Applications*, pp. 1198-1202, 2007.

[29] M. Brown, K. M. Bossley, D. J. Mills, and C. J. Hams, "High dimensional neurofuzzy systems: Overcoming the curse of dimensionality," in *Proc. IEEE International Conference on Fuzzy Systems*, vol.4, pp. 2139- 2146, 1995.

[30] C. T. Lin and C. S. George, *Neural Fuzzy Systems: A Neuro-Fuzzy Synergism to Intelligent Systems*, 1st ed., New Jersey: Prentice Hall PTR, 1996.

[31] H. Ishikawa, Y. Kamada, and H. Naitoh, "Instantaneous torque regulation for switched reluctance motors for the use in EVs," in *Proc. 2004 IEEE Workshop on Advanced Motion Control*, pp. 65-69, 2004.

[32] K. M. Rahman and S. E. Schulz, "High performance fully digital switched reluctance motor controller for vehicle propulsion," *IEEE Trans. on Industry Applications*, vol. 38, no. 4, pp. 1062-1071, 2002.

[33] D. A. Torrey and J. H. Lang, "Optimal efficiency excitation of variable-reluctance motor drives," *IEE Proc.-B*, vol. 138, no. 1, pp. 1-14, 1991.

[34] J. J. Gribble, P. C. Kjaer, and T. J. E. Miller, "Optimal commutation in average torque control of switched reluctance motors," *IEE Proc.,* vol. 146, no. 1, pp. 2-10, 1999.

[35] C. Mademlis and I. Kioskeridis, "Performance optimization in switched reluctance motor drives with online commutation angle control," *IEEE Trans. on Energy Conversion*, vol. 18, no. 3, pp. 448-457, September 2003.

[36] S. Wang and W. Lan, "Tum-on angle searching strategy for optimized efficiency drive of switched reluctance motors," in *Proc. 13th Annual Conference of the IEEE Industrial Electronics Society*, pp. 1873-1878, 2004.

[37] R. Krishnan, Switched Reluctance Motor Drives, Modeling, Simulation, Analysis, Design, and Applications, Boca Raton: CRC Press, 2001.

[38] L. E. Unnewehr and W. H. Kock, "An axial air-gap reluctance motor for variable speed applications," *IEEE Trans. On Power Apparatus and Systems*, PAS-93, pp. 367-376, 1974.

[39] T. J. E. Miller, *Electronic Control* of *Switched Reluctance Machines,* 1st ed., Oxford: Newnes Power Engineering Series, 2001.

[40] T. J. E. Miller, *Switched Reluctance Motors and Their Control*, 1st ed., New York: Magna Physics Publishing and Oxford Science Publications, 1993.

[41] T. Takahash, A. Chiba, K. Ikeda, and T. Fukao, "A comparison of output power control methods of switched reluctance motors," *PCC-Yokohama*, pp. 390-395, 1993.

[42] P. Srinivas and P. V .N. Prasad, "Voltage control and hysteresis current control of a 8/6 switched reluctance motor," in *Proc. International Conference on Electrical Machines and Systems,* pp. 1557-1562, Oct. 8~11, 2007.

[43] Z. Q. Zhu, "Electrical machines and drives for electric, hybrid, and fuel cell vehicles," *Proceedings of the IEEE*, vol.95, pp. 746-764, April 2007.

[44] G. Gallegos-L´opez, P. C. Kjaer, and T. J. E. Miller, "A new sensorless method for switched reluctance motor drives," *IEEE Trans. On Industry Applications*, vol. 34, pp. 832-840, 1998.

[45] J. H. Chen, K. T. Chau, and Q. Jiang, "Analysis of chaotic behavior in switched reluctance motors using voltage PWM regulation," *Electric Power Components and Systems*, vol. 29, pp. 211–227, 2001.

[46] L. Fausett, Fundamentals of Neural Networks: Architectures, Algorithms, and Applications, 1st ed., London: Prentice-Hall Inc., 1994.

[47] W. S. McCulloch and W. Pitts, "A logical calculus of the idea immanent in nervous activity," *Bulletin of Mathematical Biophysics*, pp. 115-133, 1943.

[48] F. Rosenblatt, "The perceptron: a probabilistic model for information storage and organization in the brain," *Psychological Review*, pp. 386-408, 1958.

[49] B. Widrow and M. E. Hoff, "Adaptive switching circuits," *IRE WESCON Convention Record*, pp. 96-104, 1960.

[50] D. E. Rumelhart, G. E. Hinton, and R. J. Williams, "Learning internal representations by error propagation," *Parallel Distributed Processing*, vol.1, pp. 675-695, 1986

[51] D. E. Rumelhart, G. E. Hinton, and R. J. Williams, "Learning representations by Back-propagating error," *Nature*, vol.323, pp. 533-536, 1986

[52] R. M. Sanner and J. J. E. Slotine, "Gaussian networks for direct adaptive control," *IEEE Trans. on Neural networks*, pp. 837-863, 1992

[53] C. T. Lin and C. S. George, *Neural Fuzzy Systems: A Neuro-Fuzzy Synergism to Intelligent Systems*, 1st ed., New Jersey: Prentice Hall PTR, 1996.

[54] M. Nørgaard, O Ravn, N. K. Poulsen, and L. K. Hansen, *Neural Networks for Modelling and Control of Dynamic Systems*, 1st ed., London: Springer-Verlag London Limited, 2000.

[55] G. W. Irwin, K. Warwick, and K. J. Hunt, *Neural Network Applications in Control,* 1st ed., London: The institution of Electrical Engineers, 1995

[56] W. Lu, "Modeling and Control of Switched Reluctance Machines for Electro-Mechanical Brake Systems," Ph.D. dissertation, Dept. ECE., The Ohio State University, Columbus, USA, 2005.

[57] J. Reinert, R. Inderka, M. Menne, and R. W. D. Doncker, "Optimizing performance in switched reluctance drives," *IEEE Industry Applications Magazine*, vol. 6, pp. 63–70, July/Aug. 2000.

[58] B. A. Kalan, H. C. Lovatt and G. Prout, "Voltage control of switched reluctance machines for Hybrid Electric Vehicles," in *Proc. IEEE 33rd Annual Power Electronics Specialists Conference*, vol. 4, pp. 1656-1660, 2002.

VITA AUCTORIS

Name   Dongyun Lu

Place of Birth   Lingbi, China

Education   *University of Windsor, Windsor, Ontario*
                      2008 - 2009
                      M.A.Sc.

                      Sichuan University, China
                      1987 -1994
                      B.Sc. and M.A.Sc.